

On the impact of modern deep-learning techniques to the performance and time-requirements of classification models in experimental high-energy physics

Giles Chatham Strong

LIP-Lisbon and Università degli Studi di Padova

`giles.chatham.strong@cern.ch`

June 5, 2022

Abstract

Beginning from a basic neural-network architecture, we test the potential benefits offered by a range of advanced techniques for machine learning and deep learning in the context of a typical classification problem encountered in the domain of high-energy physics, using a well-studied dataset: the 2014 Higgs ML Kaggle dataset. The advantages are evaluated in terms of both performance metrics and the time required to train and apply the resulting models. Techniques examined include domain-specific data-augmentation, learning rate and momentum scheduling, (advanced) ensembling in both model-space and weight-space, and alternative architectures and connection methods.

Following the investigation, we arrive at a model which achieves equal performance to the winning solution of the original Kaggle challenge, whilst requiring only 2% of the training time and 5% of the inference time using a laptop CPU instead of a GPU. Additionally, a new wrapper library for PYTORCH called LUMIN is presented, which incorporates all of the techniques studied.

Contents

1	Introduction	3
2	Higgs ML challenge	4
2.1	Challenge description	4
2.2	Current state of the art	6
2.3	Data and processing	6
2.4	Spirit of the investigation	8
2.5	Reported metrics	8
3	Solution development	9
3.1	Feature selection	9
3.2	Baseline model	15
3.3	Categorical entity embedding	16
3.4	Data symmetry exploits	18
3.5	SGD with warm restarts	19
3.6	Activation function	21
3.7	Advanced ensembling	21
3.8	Super-convergence	24
3.9	Densely connected networks	25
3.10	Architecture optimisation	26
4	Solution evaluation	30
4.1	Test results	30
4.2	Solution timing	30
4.3	Discussion	31
5	Conclusion	32
	Appendices	39
A	Parallel networks and feature splitting	39
B	Software details	45

1 Introduction

The rise of machine-learning (ML) applications has had a remarkable impact on many areas of industry and in a few academic disciplines. The field of experimental high-energy physics (HEP), however, has been slower to adopt these new approaches, with only the occasional and isolated use of basic *multivariate analyses*, such as *b*-jet tagging at LEP e.g. [1] in 1995, and $D\bar{0}$'s observation of single-top-quark production [2] in 2001; in the latter, the authors explicitly noted the importance of their neural network in fully utilising all available data to make the observation. A turning point came, however, in 2012 with the concerted use of no less than four boosted decision-trees (BDTs) in a single analysis: the search for Higgs boson decays to pairs of photons performed by the CMS collaboration at the LHC [3] - which contributed significantly to discovery of the Higgs boson by ATLAS [4] and CMS [5]. This marked a paradigm shift in the community's trust of approaches which relied less on expert knowledge.

This degree of trust had yet to extend fully to neural networks, and although they had been used to some extent at both LEP and the Tevatron, and had been outperforming other methods in other domains since 2009 (see e.g. Ref. [6] and Ref. [7]), they were still perceived as "black-box" methods; whilst researchers may be able to achieve better results by using them, they might be unable to explain how the results were achieved to sufficiently satisfy internal collaboration reviewers. In more recent years, the advancement of deep-learning approaches has led to improvements in model interpretability and greater knowledge of neural networks in the scientific community; both of which have helped foster a climate more amenable to their use [8].

Nowadays, deep neural networks (DNNs) are one of the main drivers of solutions to the domain-specific problems in HEP, such as object reconstruction[9], collision and detector simulation [10], and particle identification [11]. Although these tasks are peculiar to particle physics, their solutions normally rely on applying and adapting techniques developed outside of HEP.

Those techniques are continually being refreshed and updated, and are normally presented on benchmark datasets for some specific task, such as image recognition on ImageNet [12]. However, it is not always obvious whether improvements on such datasets would be reflected by similar success when applied in other domains. We consider this a strong motivation to study how large an improvement these new techniques can bring. To do so we will use a very well-studied, HEP-specific benchmark dataset: that of the Higgs ML Kaggle challenge [13].

In this study we examine the benefits and cross-domain applicability of several recent advances in deep-learning, including: a method to quickly optimise the learning rate; newer activation functions; learning rate scheduling; data augmentation; alternative ensembling techniques. Following these experiments we present a solution which is able to achieve consistently the performance of the winning solution, whilst requiring only 2% of the training time and 5% of the inference time using a laptop CPU instead of a GPU.

We begin with a more detailed description of both the general problem and the specific challenge (Sec. 2.1). From Sec. 3.2 through Sec. 3.10 we describe the baseline model and the various improvements, reporting performances in terms of a range of optimisation metrics. In Sec. 4 we report the final performance on the testing data, expanding to a fuller comparison with the winning solutions. The investigation and the main results are summarised in Sec. 5.

The framework and notebook experiments are made available at https://github.com/GilesStrong/HiggsML_Lumin.

2 Higgs ML challenge

In 2014 the Higgs ML challenge was launched on Kaggle (<https://www.kaggle.com/c/higgs-boson>). Participants were tasked with working on a specific kind of problem one often faces in HEP: the search for a rare signal by classification of data based on its features. The competition drew a lot of attention, with almost 2000 entries. Given the level of expertise and effort that went into the solutions, the challenge forms a viable method to benchmark models and quantitatively measure the impact of new methods and approaches. The challenge is presented in Ref. [13], and the results of the solutions are discussed in Ref. [14].

2.1 Challenge description

2.1.1 Overview

An introduction to a typical search analysis in HEP, and an overview of the specific challenge

At particle colliders such as the LHC [15], sub-atomic particles or ions are accelerated to high energies and made to collide with one another. The resulting collisions are attributable to fundamental-physics interactions between the particles, and their study can be used to compare theoretical models to reality in order to better understand the nature of the universe. The energy of these collisions gives rise to particles which are recorded with specialised instruments called *particle detectors*. Since there are many possible processes which could have given rise to a particular final state, and because the detectors only capture information of the products of the collision, there is no way to tell exactly how the final state was created. However, each of the contributing processes is likely to have some specific signature which is reflected in its outgoing products, e.g. a process which gives rise to an unstable particle will have decay products which can reconstruct its mass, but due to experimental limits, such as the finite resolution of the detector, other processes can still give rise to collisions which reproduce the signature of desired process. Effectively, the data is unlabelled with respect to the class of process which gave rise to it.

When looking to test some theory, such as the presence of a new *signal* process, one normally defines some signal-enriched region, in which the process being searched for is expected to contribute appreciably. One can then examine the rate at which events populate this region and compare it to the rate expected if the new process were not occurring and the region were only being populated by known processes (background). This is done via a test of the signal+background hypothesis against the null hypothesis of background only, e.g. using the CLs method [16]. The catch is that, due to the data being unlabelled, the background and signal rates are unknown, and only their sum is known. In some situations the signal signature (e.g. a particle mass with some determined resolution) is well known, and the background rate can be extrapolated from, or interpolated between, signal-depleted regions, but this is not always the case.

Instead, what can be done is to simulate particle collisions and the experimental equipment using a combination of analytical and stochastic modelling (see e.g. Ref [17]), a process referred to as Monte Carlo generation and detector simulation. Since one is able to generate collisions for specified processes, one now has a labelled approximation of the collider data and can estimate the signal and background rates in the signal-enriched region, applying correction factors if need be to improve the modelling and marginalising over any remaining unknown (nuisance) parameters in the hypothesis test.

The exact specification of the signal-enriched region is an important task which can have a strong influence on the outcome of a search; if the region is too wide the included signal becomes washed out by background, while if it is too narrow it may end up not

being populated at all. The main problem is the high dimensionality of the data; due to the high energy of the collisions, each collision can result in hundreds to thousands of particles, and each particle can produce multiple ‘hits’ and energy deposits in the detector. Traditionally, the first step is to reduce the dimensionality by *reconstructing* the hits and deposits back into known physics objects (fundamental particles, jets, missing energy, et cetera). The next stage is to select objects from the data which correspond to the expected final states of the signal process (and cut away events which fail to produce such objects). The signal region can then be defined using some theoretically or phenomenologically motivated function of the properties of these final states and other objects in the event.

As mentioned in Sec. 1, machine learning techniques are becoming more and more used in high energy physics analyses, due to the ease with which they can discover high-dimensional patterns in data and use them to learn to solve some problem, such as learning to separate particle collisions by class (e.g. signal or background). This ability, however, has limits and it is currently beyond our computational capacity to run such event-level classification algorithms directly on the detector recordings. The contemporary compromise is to still perform the particle reconstruction and event selection, but then to use features based on the properties of the selected particles and the event as a whole as inputs to a machine-learning based classifier and use its response to help define the signal-enriched region.

The development, training, and inference of such algorithms is still a difficult task and a source of experimentation in its own right. The Higgs ML challenge was designed to help stimulate outside interest and expertise in solving such high-energy physics problems. Participants were tasked with searching for a signal process, which was the Higgs boson decaying to a pair of tau leptons, against a background comprised of several more common processes. The competition was highly successful with 1785 teams competing, and helped to introduce many new methods to HEP, as well as produce more widely used tools, such as XGBOOST [18].

The data used in the challenge consist of simulated particle collisions, generated to mimic those expected at the LHC during its 2012 running. These are fed through a detailed GEANT 4 [19, 20]-based simulation of the ATLAS detector [21], and finally through the ATLAS reconstruction algorithms, resulting in a set of physics objects per simulated collision. These *events* are then filtered to select those compatible with containing the semi-leptonic decay of a pair of tau leptons, i.e. events which contain a hadronically decay tau lepton and either an electron or a muon. The properties of the reconstructed physics objects are then recorded in columnar-data format, with each row corresponding to a separate collision event, along with the process label and a weight used to normalise the contributions of the events. Both the label and the weight are only known due to the event being simulated.

The top solutions to the challenge made heavy use of ensembling techniques, combining tens to hundreds of models. The bases of the models were mostly either decision trees/forests, or neural networks. A lot of work seemed to go into feature engineering and selection, with a new fit-based high-level feature (CAKE¹) being developed towards the end of the competition. This appeared to improve the results for tree-based models, but gave no significant improvements to DNN-based models, indicating that sufficiently well trained networks were able to learn their own versions of it. The other focus appeared to be optimising the way in which models were ensembled, e.g regularised greedy forests [22].

¹CAKE discussion: <https://www.kaggle.com/c/higgs-boson/discussion/10329>
CAKE code: <https://bitbucket.org/tpgillam/lesterhome/src/master/>

2.1.2 Scoring metric

A statement of the scoring metric and typical optimisation of binary classifier thresholds in HEP

The performance of a solution is measured using the Approximate Median Significance [23], as computed in Eq. 1:

$$\text{AMS} = \sqrt{2(s + b + b_r) \log \left(\left(1 + \frac{s}{b + b_r} - s \right) \right)}, \quad (1)$$

in which s is the sum of weights of true positive events (signal events determined by the solution to be signal), b is the sum of weights of false positive events (background events determined by the solution to be signal), and b_r is a constant term which was set to 10 for the competition. This provides a quick, analytical value which is an approximation of the expected signal strength one would obtain after a full hypothesis test of signal+background versus background only. In High Energy Physics, an observed significance of five sigma or more can be evidence of a new discovery.

The common practice for these kinds of problems is to cut events from the data in order to remove preferentially the background events whilst retaining the signal events, in order to improve the AMS of the remaining data. Either a single cut can be used on some highly discriminating feature of the data, or multiple cuts can be used over several features. The common ML approach is to adapt the former procedure by using the features of the data to learn a new single highly discriminating feature, place a threshold on it, and then only accept events which pass the threshold. The feature learnt in this approach is simply the predicted class distribution of events, in which background events will be clustered towards zero, and signal events towards one. The AMS can then be optimised by only accepting events with a class prediction greater than some value.

The threshold cut can easily be optimised by scanning across the range of possible cuts (either at fixed steps, or checking at each data point) and picking the value which maximises the AMS. This is likely, however, to be optimal only for the dataset on which it is optimised, and performance can be expected to drop when applying the cut to unseen data. This is reflected in the challenge by requiring the solutions to predict on test data for which the class labels are not provided. It is important then that one is more careful when choosing a cut, in order to generalise better to unseen data. The approach adopted here is to consider the top 10% of events as ranked by their corresponding AMS, and compute the arithmetic mean of their class predictions and use this as the cut. This reduces the influence of statistical fluctuations in the AMS, resulting in a more generalising cut.

2.2 Current state of the art

It is our understanding that the winning solution to the Higgs ML Challenge, with an AMS of 3.80581, has yet to be outperformed under challenge conditions and so will be used as a comparison to the solution developed in this article. Whilst Ref. [24] claims to achieve an AMS of 3.979 using a method of converting the tabular data to images, in attempting to reproduce their work (https://github.com/GilesStrong/SuperTML_HiggsML_Test) we have so far only been able to reach an AMS of about 3.04 and are in contact with the authors to understand better the differences in our results.

2.3 Data and processing

A description of the dataset and preprocessing

Although the full dataset created for the challenge has now been made public [25], in order to provide an accurate comparison to the previous scores only the subset which was

used during the challenge is used here, both for training and testing. The training and testing sets consist of 250 000 and 550 000 events, respectively. Both contain a mixture of both classes: signal ($h \rightarrow \tau \bar{\tau}$); and background ($t \bar{t}$, $Z \rightarrow \tau \bar{\tau}$, and W boson decay).

Each event is characterised by two sets of training features: primary - lower level information such as tau p_T ; and derived - higher-level information calculated via (non)-linear combinations of the low-level features or from hypothesis-based fitting procedures. Tables 1 and 2 list and describe the features, and further details are available in Ref [13]. The coordinate system of the data is originally provided in terms of (p_T, η, ϕ) , however initial tests and past experience dictates that NN-based models perform better when vectors are mapped into a Cartesian coordinate system, due to the cyclical nature of the azimuthal angle, and the non-linear nature of the pseudorapidity, η :

$$\eta = \tanh^{-1} \left(\frac{p_z}{|\vec{p}|} \right),$$

where p_z is the component of 3-momenta along the beam axis, and $|\vec{p}|$ is the magnitude of the 3-momenta.

The dataset also contains information about the hardest two jets in each event. For cases in which there were not enough jets reconstructed, the features are set to default values of -999 . In order to prevent these values from having an adverse effect on the normalisation and standardisation transformations which will later be applied, these values were replaced with zeros. Similarly, any infinities or missing values (indicated by NaN) which were present in the data following the coordinate transformations were also replaced with zeros.

Since scoring the testing data requires optimising a threshold on some data, and also to provide some way to compare architectures without relying on too much on the public score of the testing data, an 80 : 20 random, stratified split² into training and validation sets is performed on the original training data. Since it was found that the validation set had a large impact on the test scores, due to the cut optimisation, experiments are repeated multiple times using different random seeds for the splitting.

After processing the data consists of 31 training features. The training data features are transformed to have a mean of zero, and a standard deviation of one. The exact same transformation is then applied to both the validation and testing data. The training and validation datasets are then each split into ten folds via random stratified splitting on the event class (signal or background). The testing data is also split into ten folds, but via simple random splitting. This was done to allow for easy training of ensembles and to make the process of augmenting the data easier. Additionally, we henceforth redefine one epoch as being a complete use of one of these folds, and during training will load each fold sequentially.

Each event in the training and validation data also contains a *weight*. This is normalised to be used to evaluate the AMS, but also reflects the relative importance of the particular event. It is a product of the production cross-section of the underlying process and the acceptance efficiency of the initial skimming procedure. Since the model is unlikely to achieve perfect classification, it is important that it focuses on learning to classify the higher weighted events better than other, less important events. This can be achieved by applying the weights as multiplicative factors during the evaluation of the loss:

$$\mathcal{L} = \frac{1}{N} \sum_{n=1}^N w_n \times \epsilon(y_n, \hat{y}_n), \quad (2)$$

²Stratified random splitting involves randomly splitting a dataset whilst ensuring that the fractional composition of events in the resulting datasets with some *stratification key* are as close as possible to those of the starting dataset. Initially this key is the event class, i.e. the ratio of signal to background in the resulting datasets matches that of the full dataset. From Sec. 3.3 onwards, the stratification key is based on the event class within categories of jet multiplicity.

where w_n is the weight associated with event n in a mini-batch of N events. This method of loss weighting is also used to account for class imbalances in the data by normalising the event weights in training data such that the sum of weights for each class are equal:

$$\sum w_{\text{signal}} = \sum w_{\text{background}} = 1. \quad (3)$$

This has the advantage of retaining the relative importance of different events within each class, whilst balancing the importance of each class overall.

2.4 Spirit of the investigation

A statement of the solution development approach

The HiggsML dataset is used due to it being a publicly accessible dataset which is representative of a typical HEP problem in both size and scoring metric, and already has strong baseline solutions from the 2014 Kaggle challenge.

The public release of the dataset now includes the truth labels of the original Kaggle test set meaning that solutions can be fully scored without requiring submissions to Kaggle. This also means that the test set can be further subdivided and mean scores computed allowing both a score and an uncertainty to be reported.

The preceding version of this investigation, available in Ref. [26], attempted to reproduce the challenge conditions by only evaluating the public score during development and then checking the private score at the end. Additionally, that investigation only considered single trainings with a fixed seed for the train/validation splitting. The investigation presented here instead attempts to evaluate the general effects that new techniques have on model performance, and so will report the mean scores from multiple trainings, each with unique random seeds for train/validation splitting. Additionally, the mean public score over ten stratified folds will be computed.

Whilst this metric would be unavailable in true challenge conditions, the final score is a product of both model optimisation and cut optimisation. Since the method to pick the cut is fixed (as per 2.1.2), the problem of *cut optimisation* reduces to *cut compatibility*. Even so, the validation AMS alone is not representative of the true performance of the method; the score on some withheld data at the chosen cut is required. Data limitations mean that it is necessary to rely on the public scores to provide some indication of true model performance. However in order to avoid overfitting to the public score, the mean score will be used, and this will be averaged over repeated trainings.

This all is to say that, although the private scores will be kept blind until the end, this investigation does not fully reproduce challenge conditions and instead aims to demonstrate the general effect of different architectures and training choices. Additionally, the solutions developed will consider the train and inference time requirements, not just performance, and hopes to produce solutions and approaches which are appropriate for use in other HEP applications.

2.5 Reported metrics

The definitions of the optimisation metrics that will be used during solution development

Several different metrics will be reported during the investigation and are averaged over six repeated trainings, each of which uses a unique train/validation splitting. The metrics are:

- The Mean Maximal Validation AMS (MMVA); the maximum AMS achievable on the validation data. MMVA can be thought of as representing an optimistic upper-limit of solution performance.

- The Mean Validation AMS at Cut (MVAC); the AMS on the validation data at the chosen cut. MVAC offers a more general measure of performance, but assumes that the cut used generalises well to unseen data.
- The Mean Averaged Public AMS (MAPA); the value of the AMS on the public part of the testing data at the chosen cut averaged over ten sub-splittings. MAPA represents a more realistic indication of performance since it accounts for cut generalisation.

MAPA will be the main metric for determining improvements, with MMVA and MVAC available to provide further indications of performance. Uncertainties computed for these metrics only account for statistical fluctuations in performance as systematic uncertainties due to theoretical modelling and experimental precision are not accounted for in the challenge.

Additionally, the time taken to train and apply each setup will be reported as the fractional increase in time compared to the baseline setup (see Sec. 3.2), and this will be averaged over the six hardware setups used. A more complete set of timings will be reported towards the end of this article.

3 Solution development

3.1 Feature selection

The definitions of the features available, and selection of the training features to use. All training features are found to be useful

As discussed in Sec. 2.3, the dataset consists of both low-level and high-level features: 18 low-level features consisting of 3-momenta, missing transverse momentum, and sum of transverse momenta of all jets; and 13 physics-inspired high-level features such as invariant masses and angles between final-state objects. Tables 1 and 2 describe the features used along with the associated name that will be used throughout this article. Figure 1 illustrates the density distributions of two example features, one high-level and the other low-level. It should be borne in mind that 3-momenta of final-states are the result of complex reconstruction techniques and so are not strictly “low-level” features, these would be the tracking hits and energy deposits in the particle detector, however they are the lowest-level of information provided in the dataset.

Our hope is that the networks will be able to exploit the low-level information, so we are interested in seeing whether all of the high-level features are necessary. Testing will use a simplified type classification model called a Random Forest [27]. We use these as they are quick and easy to train, provide decent performance, and do not require the data to be transformed in any particular fashion prior to training.

In the feature selection we train five Random Forests to classify signal and background events using only the high-level features. We then use these models to calculate the permutation importance of each of the high-level features by averaging the importance over the five models, which are shown in Fig. 2. From this, we can see that all features except the four nearest the top of the plot, i.e. those associated with jet pairs, appear to be important (considering a permutation importance greater than 0.005 as “important”).

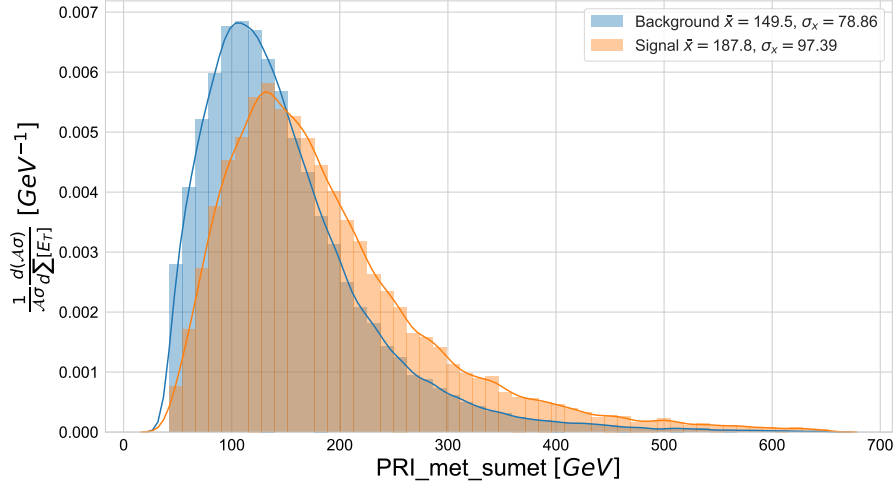
The lack of importance of jet-pair features is to be expected: since the majority of events do not contain two or more jets, the values for these features are often the default value of zero. When the feature is permuted, most of the zeros will be replaced with another zero, and the model response remains mostly unaffected. Effectively the di-jet features are only important for a subset of events, but their importance is smeared out across all events. In actual application, the jet number will be encoded in a way such that the model will be able to more easily target these di-jet events and make use of their

Feature name	Description	Grouping
DER_mass_MMC	Mass of the Higgs boson estimated by a hypothesis based fitting technique	Mass, Higgs
DER_mass_transverse_met_lep	Transverse mass of the lepton and \vec{p}_T^{miss}	Mass, Higgs
DER_mass_vis	Invariant mass of the lepton and the tau a naïve estimate of the mass of the Higgs boson	Mass, Higgs
DER_pt_h	Transverse momenta of the vector sum of the lepton, tau, and \vec{p}_T^{miss}	3-momenta, Higgs
DER_deltaeta_jet_jet	Absolute difference in pseudorapidity of the leading and subleading jets (undefined for less than two jets)	Angular, Jet
DER_mass_jet_jet	Invariant mass of the the leading and subleading jets (undefined for less than two jets)	Mass, Jet
DER_prodelta_jet_jet	Product of the pseudorapidities of the leading and subleading jets (undefined for less than two jets)	3-momenta, Jet
DER_deltar_tau_lep	Separation in $\eta - \phi$ space of the lepton and the tau	Angular, Final-state
DER_pt_tot	Transverse momentum of the vector sum of the transverse momenta of the lepton, tau, the leading and subleading jets (if present), and \vec{p}_T^{miss}	Sum, Final-state
DER_sum_pt	Sum of the transverse momenta of the lepton, tau, and all jets	Sum, global event
DER_pt_ratio_lep_tau	Transverse momenta of the lepton divided by the transverse momenta of the tau	3-momenta, Final-state
DER_met_phi_centrality	Centrality of the azimuthal angle of \vec{p}_T^{miss} relative to the lepton and the tau	Angular, Final-state
DER_lep_eta_centrality	Centrality of the pseudorapidity of the lepton relative to the leading and subleading jets (undefined for less than two jets)	Angular, Jet

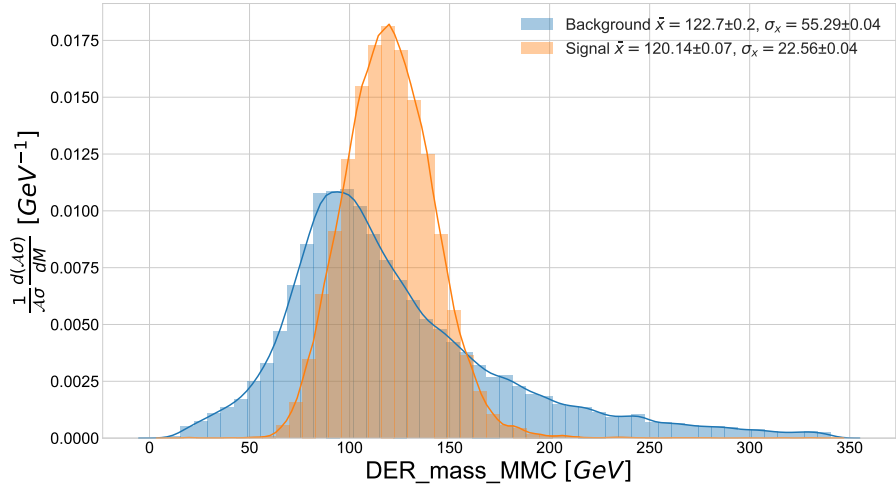
Table 1: Glossary of high-level (derived) features used for training, along with their grouping.

Feature name	Description	Grouping
PRI_tau_[px/py/pz]	3-momenta of the tau in Cartesian coordinates	3-momenta, Final-state
PRI_lep_[px/py/pz]	3-momenta of the lepton in Cartesian coordinates	3-momenta, Final-state
PRI_met_[px/py]	Components of the vector of missing transverse momentum in Cartesian coordinates	3-momenta, Final-state
PRI_met	Modulus of the vector of missing transverse momentum in Cartesian coordinates	3-momenta, Final-state
PRI_met_sumet	Sum of all transverse energy	Energy, Final-state
PRI_jet_num	Number of jets in event	Multiplicity, Jet
PRI_jet_leading_[px/py/pz]	3-momenta of the leading jet in Cartesian coordinates (undefined if no jets present)	3-momenta, Jet
PRI_jet_subleading_[px/py/pz]	3-momenta of the subleading jet in Cartesian coordinates (undefined if more than two jets present)	3-momenta, Jet
PRI_jet_all_pt	Sum of transverse momenta of all jets in Cartesian coordinates	3-momenta, Jet

Table 2: Glossary of low-level (primary) features used for training, along with their grouping. Note that `PRI_jet_all_pt` can be expected to be different from the sum of p_T of leading and subleading jets, since there can be events which contain more than two jets, however the dataset only contains details of the two jets with the highest p_T .



(a) Example low-level feature: the sum of missing transverse energy ($\sum E_T$)



(b) Example high-level feature: the masses of the Higgs candidates as computed by a hypothesis-based fitting algorithm ($M_{\tau\tau,MMC}$)

Figure 1: Example distributions for low-level and high-level features in the data.

features. The di-jet features will therefore be kept. As additional motivation, training a new Random Forest without these features showed a drop in performance on unseen data.

In order to check for monotonic relationships between features we then compute the Spearman’s rank-order correlation coefficients [28] for every pair of high-level features and do not find any pairs which were fully (anti-)correlated with one another. As a final check we examine the mutual dependencies of the features, i.e. how easy it is to predict the value of a feature using the other features as inputs to a Random Forest regressor. As shown in Fig. 3, none of the non-di-jet high-level features are completely predictable using the other features (dependencies are never equal to one). We can therefore expect that each high-level feature is bringing at least some unique information not carried by the others.

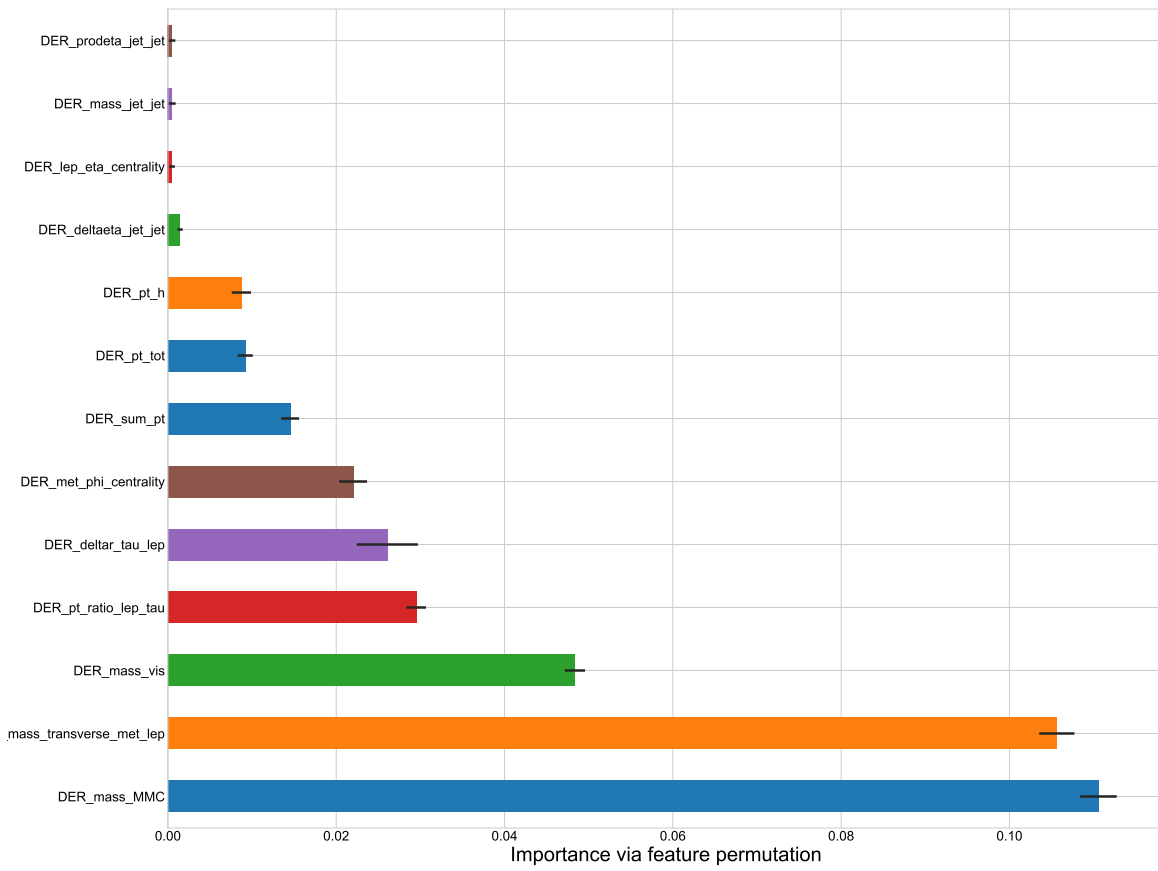


Figure 2: Illustration of the fractional permutation importance of the high-level features as estimated using the average importance over five Random Forest models.

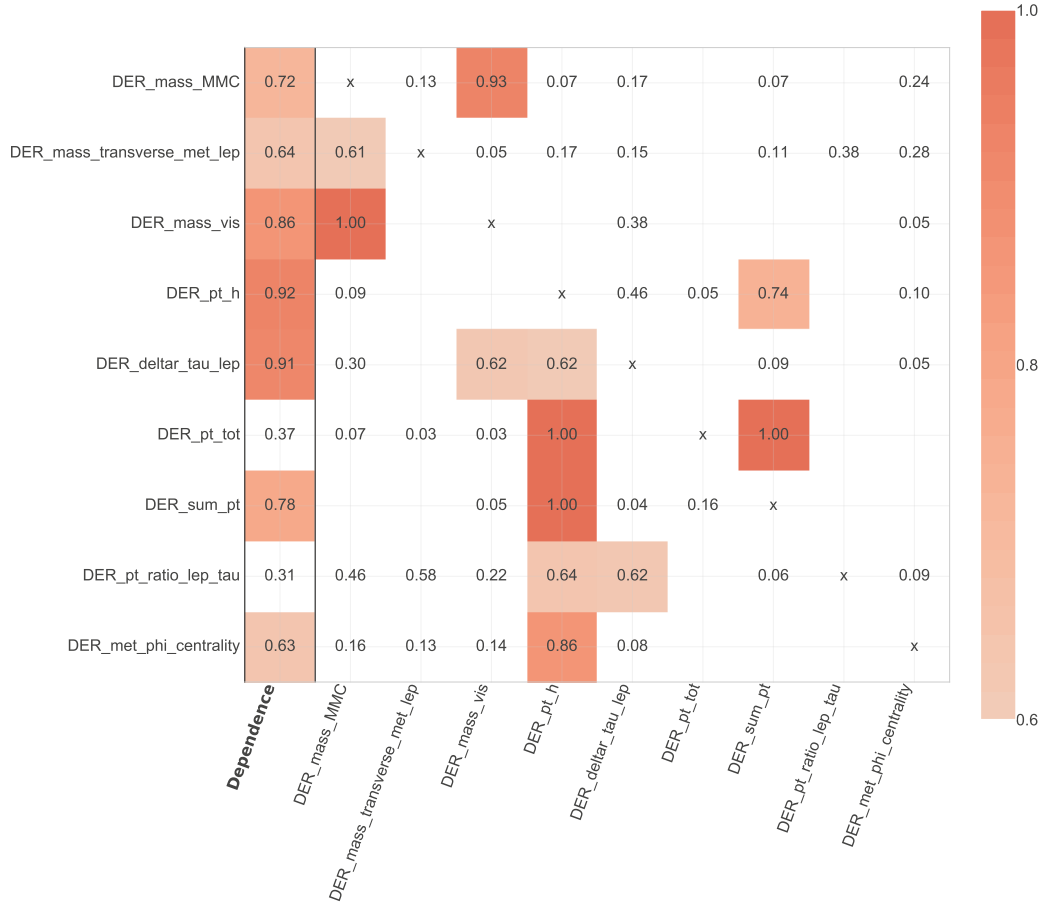


Figure 3: Illustration of feature dependence and associated feature importance using Random Forest regression. Considering each row separately, the feature on the y axis is one being regressed to. The value in the "Dependence" column is the coefficient of determination (R^2); higher means easier to predict the feature values. The remaining columns indicate how much each feature on the x axis contributes to the performance of the regressor; higher means more important. As an example: *DER_pt_h* is the easiest feature to predict (dependence of 0.92), and *DER_sum_pt* is moderately important to the regressor.

3.2 Baseline model

The basic architecture and a demonstration of the benefits of ensembling models

Training and inference of all solutions developed in this article are performed in LUMIN [29], a wrapper library for PYTORCH, which so far has been primarily developed by the author of this article.

3.2.1 Architecture

The baseline model consists of a simple neural network architecture. Specifically, it contains: Four fully-connected layers, each of 100 neurons, with weights initialised according to the He-normal [30] scheme. ReLU activation functions [31] follow each fully-connected layer. The output layer consists of a single neuron, whose weights are initialised according to the Glorot-normal [32] scheme. A sigmoid activation function is applied to the output of the network. The starting biases for all layers are set to zero.

As usual, the parameters (weights and biases) of the network are optimised through backpropagation [33] of a loss-gradient estimated by averaging batches of data points (here we use a minibatch size of 256 events). Given that the problem involves binary classification, the loss function is chosen to be the binary cross-entropy of network predictions. The update steps are determined using ADAM [34] with relatively standard parameter settings of $\beta_1 = 0.9$, $\beta_2 = 0.999$, and $\epsilon = 1 \times 10^{-8}$. The learning rate (LR) is kept constant during training at 2×10^{-3} , which was found using a LR Range Test as described in Ref. [35]. Training continues until the loss on a validation fold of the training data has not decreased in the last 50 epochs, after which the model state corresponding to the lowest validation loss is loaded.

3.2.2 Performance

Single model A single model is trained on nine out of the ten training folds, with the tenth fold acting as validation data for loss monitoring. Once finished, the model is applied to both the validation and testing data, and the required metrics recorded. This process is repeated six times on six different hardware setups, each using a unique random seed for the train/validation splitting as described in Sec. 2.3. Performance metrics for the single model are reported in Tab. 3.

Ensemble An ensemble of ten models is trained, again using nine out of the ten training folds, with the tenth fold acting as validation data. Each model uses a different fold of the training data for validation. The resulting models are ensembled by weighting their predictions proportionally to the inverse of their associated loss on their validation folds, i.e. models which reached a lower validation loss during training have a greater influence over the ensemble prediction than those with a higher loss.

Ensembling is seen to provide improvements in all metrics compared to the single model setup. With expected increases in train and inference time. Note that the inference-time increase appears to be sub-linear due to the fact that the data are kept in memory between model evaluations. Based on the improved performance, we proceed to adopt the ensembled version as the baseline model for later comparisons.

Setup	MMVA	MVAC	MAPA	Fractional time-increase	
				Training	Inference
Single model	3.43 ± 0.04	3.38 ± 0.04	3.44 ± 0.02	-	-
Ensemble	3.70 ± 0.05	3.64 ± 0.04	3.664 ± 0.007	10.4 ± 0.6	5.9 ± 0.9

Table 3: Validation-performance comparison between using the single model and weighted ensemble setups. Higher values of MMVA, MVAC, and MAPA indicate better performance, and higher values of fractional time-increase indicate that the solution takes longer to train and/or apply. The best values for each metric are shown in bold, and the setup chosen is also indicated in bold.

3.3 Categorical entity embedding

The testing of an efficient way to encode categorical information, which results in mild improvements

In Sec. 3.2 we considered all features in the data to be continuous variables, however the number of jets in an event (`PRI_jet_num`) could instead be thought of as a categorical feature. Although two jets are more than one jet, this can also be treated as defining subcategories of particle interactions, e.g. a two-jet event and a one-jet event, in which case there is no longer a numerical comparison. Optimal treatment of categorical features requires encoding the different categories in a way such that the ML algorithm can easily access them individually. A common way to do this is to assign each category an integer code which begins at zero and sequentially increases, and then treat these codes as row indices of an *embedding* matrix. The elements in the indexed row are then used to represent the corresponding category.

Under the *1-hot encoding* scheme, the embedding matrix is a $N \times N$ identity matrix (where N is the number of categories in a feature; its *cardinality*), i.e. each category is represented by a vector of length N in which only one value is non-zero (one element is *hot*). Whilst this approach provides unique access to each category, the number of input variables is now N . For high cardinality features, or many low-cardinality features, this can quickly lead to a huge increase in the number of model parameters which must be learnt.

Reference [36] instead suggests for neural networks to use an $N \times M$ weight matrix for the embedding, where $M < N$ is a hyper-parameter which must be chosen. Each category is now represented by a real-valued vector of length M , i.e. in a more compact fashion than 1-hot encoding would provide. The values of the weight matrix are then learnt via backpropagation during training. This approach of *categorical entity embedding* works because, for example, it is likely that it is more important to know whether an event contains zero, one, several, or many jets, rather than exactly how many jets, but rather than manually compacting the categories (and having to define a priori “several” and “many”), a compact, information rich, and task specific representation can be learnt. The additional hyper-parameter M can be estimated using domain knowledge or by using some rule-of-thumb: the original paper suggests to use $M = N - 1$, and FASTAI suggests to use half the feature cardinality or 50, whichever is smaller ($M = \min(50, (N + 1) // 2)$ [37])

For embedding `PRI_jet_num`, M is chosen to be three and initial weights for the 4×3 matrix are sampled from a unit-Gaussian distribution. As shown in Tab. 4, this is found to provide metric improvements across the board, for only minor increases in train and inference time. Figure 4 shows an example of one of the learned embeddings.

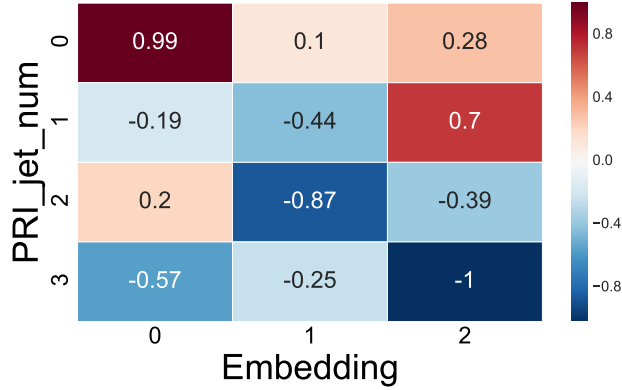


Figure 4: Illustration of an example of a learned embedding matrix for the number of jets. Note that each row is unique, indicating that the NN found it useful to learn separate embeddings for each category, and was able to transform the feature into a lower dimensional representation.

Setup	MMVA	MVAC	MAPA	Fractional time-increase	
				Training	Inference
Baseline	3.70 ± 0.05	3.64 ± 0.04	3.664 ± 0.007	-	-
+Embedding	3.78 ± 0.05	3.70 ± 0.06	3.71 ± 0.02	0.13 ± 0.03	0.08 ± 0.04
+Augmentation	3.96 ± 0.04	3.89 ± 0.05	3.79 ± 0.01	1.45 ± 0.08	14 ± 5
+SGDR	3.94 ± 0.06	3.90 ± 0.04	3.80 ± 0.02	2.12 ± 0.07	14 ± 5
+Swish	3.96 ± 0.06	3.86 ± 0.05	3.81 ± 0.02	2.32 ± 0.07	17 ± 4
-SGDR + SWA	3.96 ± 0.06	3.88 ± 0.05	3.81 ± 0.02	2.03 ± 0.07	17 ± 4
-SWA + 1cycle	4.04 ± 0.06	3.85 ± 0.04	3.81 ± 0.02	0.66 ± 0.04	17 ± 4
+Dense	3.95 ± 0.04	3.89 ± 0.05	3.82 ± 0.02	0.81 ± 0.08	17 ± 5

Table 4: A summary of solution evolution in terms of the optimisation metrics and the time impact. Fractional time-increases are computed with respect to the baseline model, which is the ensembled solution from Sec. 3.2. This table includes all improvements that are discussed in this article, and so contains solutions which may not have been introduced at time of reading. A ‘+’ indicates the addition of a new method to the solution, and ‘-’ indicates the removal of a previously added method. The best values for each metric are shown in bold, and the setup chosen is also indicated in bold.

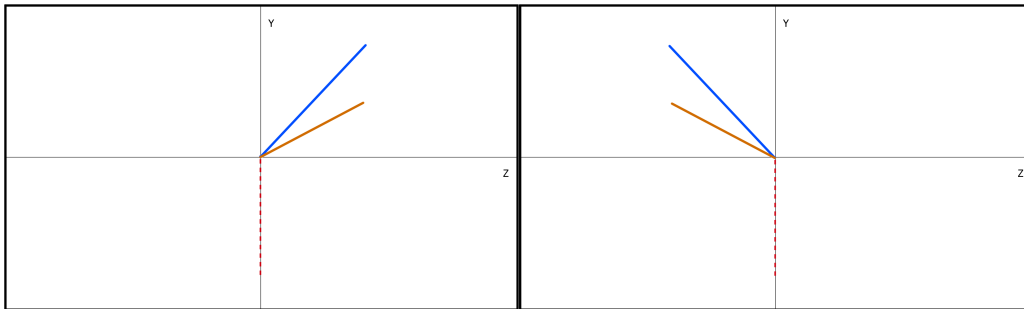
3.4 Data symmetry exploits

Discussion and application of HEP-specific data augmentation, which result in large improvements

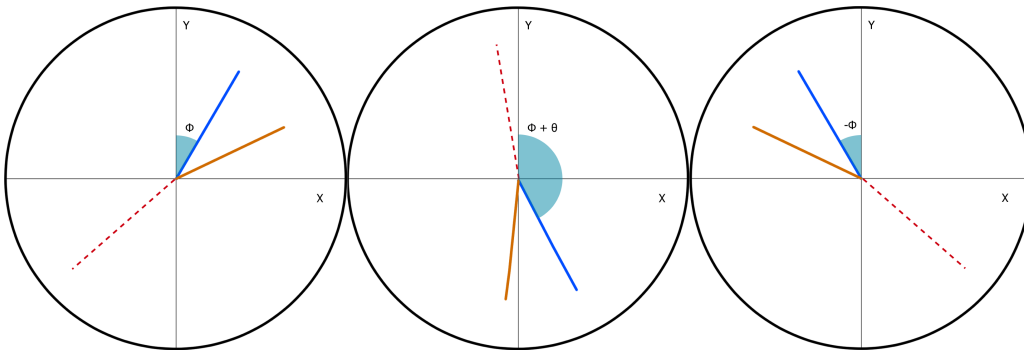
3.4.1 Overview of data symmetries

At particle colliders such as the LHC [15], beams of particles with the same quantum numbers collide head-on with approximately zero transverse momentum. Because of this the resulting final states can be expected to be produced isotropically in both the transverse plane (x, y) and the longitudinal axis (z). Particle detectors such as CMS [38] and ATLAS [21] are built to account for these isotropies by being symmetric in both azimuthal angle (ϕ) and pseudorapidity (η). All this is to say that the class of physical process which gave rise to the collision event is only related to the relative separation between the final states, and not the absolute position of the event.

Since the data used in this problem are simulated for such a collider and detector combination, the class is invariant to flips in the transverse or longitudinal planes, and to rotations in the azimuthal angle, as illustrated in Fig. 5.



(a) Left: an example event in the $y-z$ plane, with blue and orange lines representing arbitrary final-state vectors and the dashed line representing missing transverse momentum. Right: the same event having been flipped in the longitudinal axis.



(b) Left: an example event in the transverse plane, with blue and orange lines representing arbitrary final-state vectors and the dashed line representing missing transverse momentum. Centre: the same event having been rotated in the azimuthal angle (ϕ). Right: the same event having been flipped in the y axis.

Figure 5: Illustrations of class-preserving transformations for particle collisions.

3.4.2 Data fixing

The existence of class-invariant symmetries in the data acts to increase the data complexity; a classifier must learn to become invariant to the absolute orientation of events and

Setup	MMVA	MVAC	MAPA	Fractional time-increase	
				Training	Inference
Fixing	3.90 ± 0.04	3.83 ± 0.05	3.76 ± 0.01	-	-
Augmentation	3.96 ± 0.04	3.89 ± 0.05	3.79 ± 0.01	1.11 ± 0.05	13 ± 5

Table 5: Comparison of data symmetry exploits in terms of the optimisation metrics and time impact. The best values for each metric are shown in bold, and the setup chosen is also indicated in bold.

instead focus on the positions of the particles relative to one-another. This complexity can easily be removed by rotating all events to have a common alignment.

We refer to this pre-processing step as *data fixing*, and implement it by first rotating events in the transverse plane and reflecting in the longitudinal plane such that the light-leptons (`PRI_lep`) are at $\phi = 0$ and $\eta \geq 0$, and then reflecting the event in the transverse plane such that the tau leptons (`PRI_tau`) are in the positive ϕ region. Since the y component of the light-lepton’s 3-momentum is now constant (zero) it can be dropped as an input feature during training.

3.4.3 Data augmentation

An alternative approach to dealing with the data symmetry is instead to exploit it as a means of generating augmented copies of events. Data augmentation is a common technique for improving the generalisation power of a model. It involves applying class-preserving transformations to the data in order to exploit or highlight certain invariances between the input and target features. In the field of image classification, these transformations could be small rotations, flips, zooms, or colour and lighting adjustments, e.g. Ref. [39]. The data augmentation applied here consists of event flips in the y and z planes and rotations in the transverse plane. Application of the augmentations may be done during training in order to artificially inflate the size of the training data (train-time augmentation), or during inference by taking the mean prediction for a set of augmentations (inference-time augmentation).

Train-time augmentation was performed by applying a random set of augmentations before each data point is used (implemented by augmenting each fold when loaded). Inference-time augmentation was performed by taking the mean prediction for each data point over a set of eight transformations: each possible combination of flips in y and z for two different ϕ orientations (original ϕ and $\phi + \pi$).

3.4.4 Comparison

Table 5 compares the two approaches in terms of the optimisation metrics. Data augmentation produces more favourable scores, but at the expense of a large increase in inference time. Nevertheless, the absolute inference time is still acceptable (15s on a GPU and 2min on the slowest CPU), so the augmentation approach was chosen going forwards. Table 4 compares the improvements against the baseline solution.

3.5 SGD with warm restarts

Testing of learning-rate annealing schedules. Whilst this results in moderate improvements it eventually becomes obsolete by the schedule in Sec. 3.8

According to Ref.[40], the learning rate (LR) is one of the most important parameters to set when training a neural network. Whilst initial, optimal values can be found using

a LR Range Test [35], it is unlikely that this will remain optimal throughout training. A common approach is to decrease the LR in steps [41] during training (either at preset points or when the loss reaches a plateau).

Reference [42] instead proposes a *cosine-annealing* approach in which the LR is decreased as a function of mini-batch iterations according to half a cycle of a cosine function. This means that initial training is performed at high LRs, where the model can quickly move across the loss surface towards a minima, and the final training is spent at lower LRs allowing the model to converge to a minima, with a smooth, approximately linear transition between these states. Additionally, by repeating this cosine decay, the paper suggests that the rate of convergence can be further improved, a process described as *warm restarts*.

Reference [43] suggests these sudden changes in the LR allow the model to explore multiple minima. This exploration of minima could in turn lead to the discovery of wider, less steep minima, which should generalise better to unseen data since changes in the centre of the minima will have less of an effect on the loss than if the minima were steeply sided.

Figure 6 illustrates the LR schedule and an example of the validation-loss evolution.

1. We begin at an initial LR, γ_0 , of 2×10^{-3} and an initial cycle length, T , of one complete use of the training folds.
2. During the cycle, the LR is decreased according to $\gamma_t = 0.5 \gamma_0 \times (1 + \cos(\pi t/T))$, where t is incremented after each minibatch update
3. Once the LR would become zero ($t = T$), t is reset to zero, resulting in a sudden increase in the LR (the warm restart). Additionally, the cycle length T is doubled allowing the model to eventually spend longer and longer time at lower LRs, improving convergence.

The warm restarts are visible in the validation loss, appearing as small increases in the loss. Initially, the early stopping criterion was modified such that training stopped once the model went one entire cycle without an improvement in the validation loss, however since testing showed models always reached this point in the same annealing cycle, the number of training epochs was instead fixed to avoid unnecessary training time.

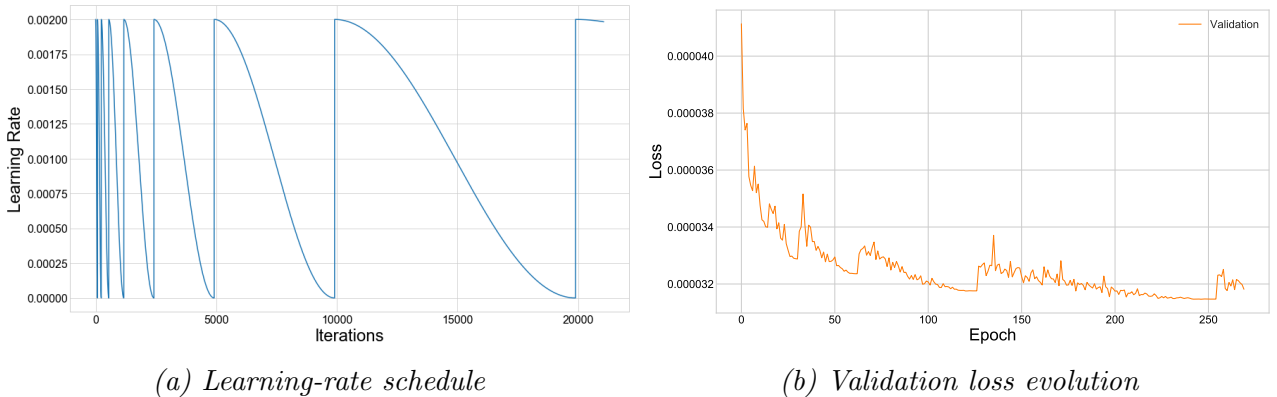


Figure 6: Cosine annealed learning-rate schedule with increasing cycle length and example of the corresponding loss evolution for a model trained with such a schedule

The results (Tab. 4) show a minor improvement in both MVAC and MAPA, and a decrease in MMVA, indicating a less overly optimistic solution with better generalisation.

3.6 Activation function

The inclusion of a newer activation function, which provides slight improvements

Whilst ReLU is a good default choice for an activation function, it does exhibit several problems, which more recent functions attempt to address:

- The Parametrised ReLU (PReLU) [30] is similar to ReLU, but can feature a constant, non-zero gradient for negative inputs, the coefficient of which is learnt via backpropagation during training;
- The *Scaled Exponential Linear Unit* (SELU) [44] uses careful derived scaling coefficients to keep signals in the network approximately unit Gaussian, without the need for manual transformation via batch normalisation [45]. It is recommended to use the `lecun` initialisation scheme [46] for neurons using the SELU activation function;
- The Swish function [47] was found via a reinforcement learning based search, and features the interesting characteristic of having a region of negative gradient, allowing outputs to decrease as the input increases: $\text{Swish}(x) = x \cdot \text{sigmoid}(\beta x)$, where β can either be kept constant or be learnt during training. The recommended weight initialisation scheme for Swish is the same as the one for ReLU, i.e. He.

A comparison of these functions is shown in Fig. 7.

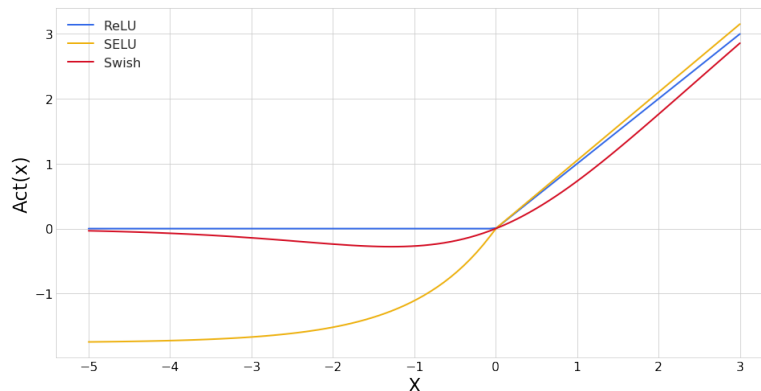


Figure 7: Responses ($\text{Act}(x)$) for several activation functions for a range of input values, x . PReLU (not shown) is the same as ReLU in the positive region, $\text{Act}(x) = x$, and with a constant, non-zero gradient in the negative region, $\text{Act}(x) = \alpha x$, where α is a parameter of the model

Previous testing, documented in Ref. [26], found that the Swish activation function provided superior performance, and so its improvements were again tested here. We use the Swish-1 version, in which $\beta = 1$ and is not changed during training. As shown in Tab. 4, its inclusion provides slight improvements to MAPA, and so its use was accepted. Note that the small time increase is due to the exponentials in Swish being more complicated to compute than the `max` operation of ReLU.

3.7 Advanced ensembling

A discussion and experimental test of several more complicated methods of build an ensemble of models. Additionally a new implementation of Stochastic Weight Averaging is introduced which does not rely on a predefined starting point. Whilst this provides slight improvements in training time it is eventually made obsolete by the schedule in Sec. 3.8

As mentioned in Sec. 3.5 Ref. [43] suggests that Ref. [42]’s process of restarting the LR schedule allows the network to discover multiple minima in the loss surface. The paper builds on this by introducing a method in which an ensemble of networks results from a single training cycle by saving copies of the networks just before restarting the LR schedule, i.e. when the model is in the minima. This process of *Snapshot Ensembling* (SSE) is further refined into *Fast Geometric Ensembling* (FGE) in Ref. [48], by forcing the model evolution along curves of constant loss between connected minima (simultaneously and independently discovered by Ref. [49]).

The problem with these methods is that whilst they allow one to train an ensemble in a much reduced time, one still has to run the data through each model individually, so the application-time is still increased. Reference [50] instead finds an approach which leads to an approximation of FGE in a single model. This is done by averaging the models in *weight space*, rather than in *model space*. The general method involves training a model as normal, until the model begins to converge. At this point the model continues to train as normal, but after each epoch a running average of the model’s parameters is updated.

In the training, one has to decide on when to begin collecting the averages: *too early*, and the model average is spoiled by ill-performing weights; *too late*, and the model does not explore the loss surface enough to allow SWA to be of use. Additionally, SWA may be combined with a cyclical learning rate, in which case weight averaging should take place at the end of each cycle.

3.7.1 Implementation

SSE SSE was tested by training ten networks as usual, with a cosine-annealed LR (initial LR = 2×10^{-3}) with a constant cycle length of 50 folds. Training continued until the validation loss failed to decrease for two complete cycles. Snapshots were then loaded, starting with the best performing set of weights, and then up to four previous snapshots. A weighting function of the form $w = n^{-1}$ was used, where n is the 1-ordered number of weight loads (i.e. best performing weights = 1, first previous snapshot = 2, et cetera). This means that snapshots later in the training are weighted higher than earlier ones, in order to balance the trade off between greater generalisation due to a larger ensemble being used and the poorer performance of earlier snapshots. Additionally snapshots loaded from different model trainings were not reweighted according to validation loss as they were in Sec. 3.2.

FGE Since FGE expects to send models along curves of near constant loss between minima, it employs a higher frequency saving of snapshots. A linearly cycled LR [35] is used, moving from LR = 2×10^{-4} to 2×10^{-3} and back again over the course of five folds. Training continued until the validation loss had not decreased for nine cycles. Snapshots were loaded in a similar fashion to SSE except up to 8 cycles, as well as the best performing weights, were loaded, and no cycle weighting was used (the losses of the cycles were approximately equal, as expected).

SWA Rather than having to pick a starting point to begin SWA (which would require running the training once beforehand without SWA, SWA was begun early during training and later a second average was tracked. At set points during training the SWA averages were compared. if the older average performed better, then the younger average was reset and the time to the next comparison was doubled. If the younger average was better, then the older average was reset and the time to the next comparison was set back to its initial value (its *renewal period*). Effectively, a range of possible start points for SWA are tested, and the optimum start position is automatically selected.

Additionally, three LR schedules were tested:

Setup	MMVA	MVAC	MAPA	Fractional time-increase	
				Training	Inference
Current solution	3.96 ± 0.06	3.86 ± 0.05	3.81 ± 0.02	-	-
SSE	3.95 ± 0.05	3.85 ± 0.05	3.81 ± 0.02	0.15 ± 0.03	1.5 ± 0.3
FGE	3.95 ± 0.06	3.86 ± 0.05	3.80 ± 0.02	-0.13 ± 0.03	6 ± 1
SWA constant	3.96 ± 0.06	3.88 ± 0.05	3.81 ± 0.02	-0.09 ± 0.01	-
SWA linear cycle	3.97 ± 0.06	3.87 ± 0.04	3.81 ± 0.02	0.25 ± 0.03	-
SWA cosine	3.95 ± 0.05	3.89 ± 0.05	3.81 ± 0.02	0.22 ± 0.04	-

Table 6: Comparison of the various advanced ensembling approaches. “Current solution” refers to the solution as of Sec. 3.6. The best values for each metric are shown in bold, and the setup chosen is also indicated in bold.

- A constant LR of 2×10^{-3} running with a patience of 50 folds with SWA beginning on the fifth fold, and comparisons between averages taking place with an initial separate of five folds.
- A Cosine annealed LR between 2×10^{-3} and 2×10^{-4} over five folds, a patience of 9 cycles, and SWA beginning on the second cycle with a renewal period of two cycles.
- A linearly cycled LR between 2×10^{-4} and 2×10^{-3} over five folds, a patience of 9 cycles, and SWA beginning on the second cycle with a renewal period of two cycles.

3.7.2 Comparison

Comparing the approaches to the current best solution in Tab. 6, we can see that no approach is able to improve the current MAPA, however SWA with a constant LR achieves the same score in a shorter train time. From an example plot of the validation loss over time (Fig. 8) we can see that SWA not only demonstrates better performance, but it also shows a heavy suppression of loss fluctuations and converges to a loss plateau, where as the non-averaged model eventually over-fits (signified by an increasing loss in the later stages of training). The sharp drops in SWA loss are due to the old average being replaced with the newer average.

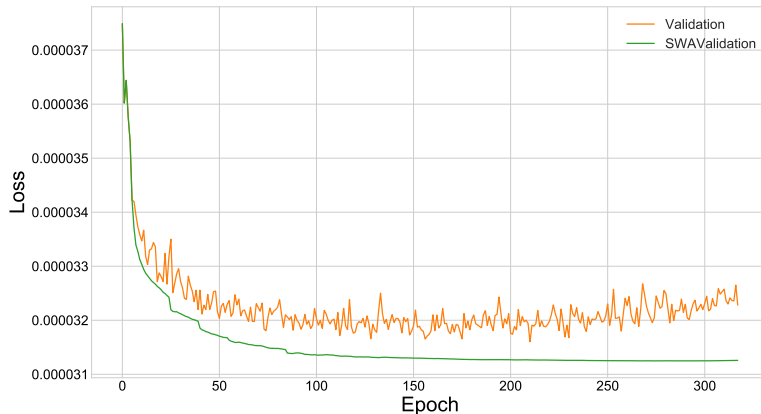


Figure 8: Example evolution of validation loss over training time for both model being trained and the stochastic weight-average of the model states.

3.8 Super-convergence

The development of a schedule for both learning rate and momentum which provides a significant reduction in training time

Reference [51] introduces the concept of *super convergence*, in which a specific LR schedule, *1cycle*, is used to achieve convergence much quicker (between five and ten times) than traditional schedules allow. This is further discussed in Ref. [52]. The 1cycle policy combines both cyclical LR and cyclical momentum (or β_1 in case of ADAM), and evolves both hyper-parameters simultaneously, but in opposite directions (LR initially increasing, momentum initially decreasing), over the course of training in a single cycle, i.e. when the LR is at its maximum, the momentum is at its minimum. In this way the two parameters help to balance each other, allowing the use of higher learning rates without the network becoming unstable and diverging. In the final stages of training, the LR is allowed to decrease several order of magnitude below its initial value.

One of the key points of Ref. [52] is that super-convergence can only occur if the amount of regularisation present in the setup is below a certain amount, but that once super-convergence can be achieved, other forms of regularisation can then be tuned accordingly. In our current setup, we have avoided explicitly adding tuneable forms of regularisation for this reason. However Sec. 3.4’s choice to use data augmentation rather than data fixing equates to choosing not to reduce regularisation through data complexity. Because of this, we will be conservative in our testing of super-convergence and attempt to only halve our training time.

Implementation of 1cycle follows the suggestion of Fast.AI [53], in which the halves of the cycles are half-cosine functions, rather than linear interpolations. This can be expected to offer the same advantages of the cosine annealing schedule of Ref [42] and also provide a smooth transition between the directions of parameter evolution. The total length of the cycle was set to 135 folds (approximately half that required for the solutions of Sec. 3.5 and Sec. 3.7). The lengths of the first and second parts of the cycle were set to 45 folds and 90 folds, respectively, i.e. a ratio of 1:2, allowing a longer time for final convergence. Based on a LR range test performed at a constant β_1 of 0.9 and the knowledge that β_1 would be at a minimum when the LR is maximised, a slightly higher maximum LR of 1×10^{-2} and an initial value of 1×10^{-4} were chosen.

As shown in Fig. 9, during the first part of the cycle, the LR is increase from its initial value (1×10^{-4} to its maximum of 1×10^{-2} while β_1 is decreased from 0.95 to 0.85. In the second half, β_1 returns back up to 0.95, but the LR is allowed to tend to zero. As shown in Tab. 4, although 1cycle provides the same level of MAPA performance as SWA, it is able to reach this level of performance in half the time.

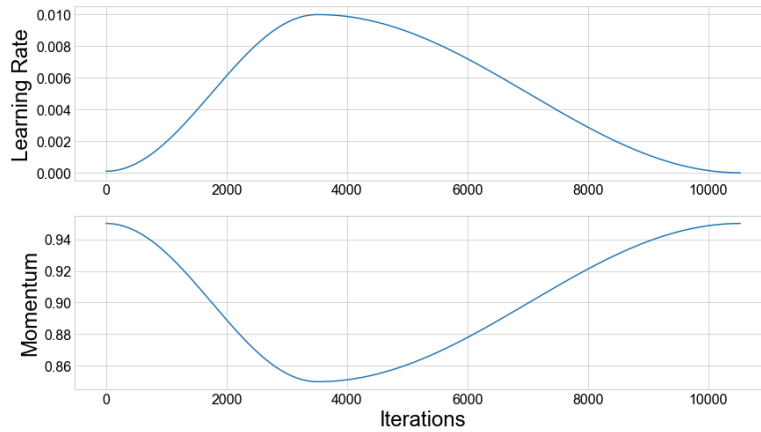


Figure 9: Illustration of the evolution schedule of the learning rate and momentum (β_1) used during testing. Iterations are minibatch updates.

3.9 Densely connected networks

An investigation into different connections between layers, which is found to provide a mild improvement in performance whilst reducing the number of free parameters in the networks

The fully-connected architectures used so far aim to learn a better representation of the data at each layer, however this means that potentially useful information is lost after each layer if it has not been sufficiently well represented by the latest layer. Being able to do so requires that the layers have a sufficient number of free parameters to avoid losing useful information. Due to limited training data, this limits the depth of the networks which can be trained and so potentially limits the performance of the model.

In their 2016 paper, “Densely Connected Convolutional Networks” [54], Huang and Weinberger present an architecture in which, within subgroups of layers, the outputs of all previous layers are fed as inputs into all subsequent layers via channel-wise concatenation. This means that lower-level representations of the data are directly accessible by all parts of the block. This potentially both allows a more diverse range of features to be learnt, and for layers to be trained via *deep supervision* [55] due to more direct connections when back-propagating the loss gradient. Additionally, it means that the weights which were previously required to encode the low-level information may no longer be necessary.

Whilst the paper presents this dense connection in terms channel-wise concatenation of the outputs of convolutional filters, the same idea can be applied to fully connected networks by concatenating width-wise the output tensor of each linear layer with the that layer’s input tensor; i.e. $x_{i+1} = D_i(x_i) \oplus x_i$, where x_i is the hidden state before the i^{th} linear layer (D_i), as illustrated in Fig. 10.

3.9.1 Testing

The architecture up to now has used four hidden layers, each with 100 neurons. Including the embedding and output layers, the total number of free parameters is 33 813 . For the densely connected architecture we reduce the width of linear layers to 33 (the number of continuous inputs plus the width of the categorical embedding output), and increase the depth of the network to six hidden layers. The outputs of each hidden layer except the last are concatenated with their inputs to compute the input tensor to the next hidden layer. This results in a total of 23 113 free parameters, i.e. about two thirds of the original size.

Training of the networks used the same 1cycle schedule as presented in Sec. 3.8. As

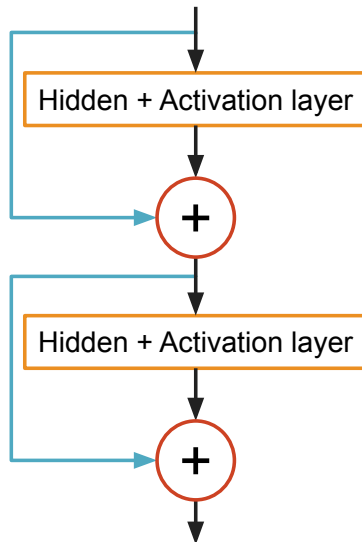


Figure 10: Illustration of a densely-connected, non-convolutional network. \oplus indicates concatenations of hidden states.

shown in Tab. 4, the densely connected architecture provides mild improvements in both MVAC and MAPA, despite being significantly smaller, however due to the extra depth and concatenation operations, training and inference timing is approximately the same as the previous architecture.

3.10 Architecture optimisation

A random search over the remaining hyper-parameters to finalise the model. Interestingly the existing architecture is found to work best and the model displays only a weak dependence on its hyper-parameters

3.10.1 Overview of remaining considered hyper-parameters

The solution choices made so far equate to rough optimisation of hyper-parameters and training-method choices, but the underlying architecture of the network has remained relatively constant. For the final stage of solution optimisation, we explore the impact of adjusting the remaining hyper-parameters: number of hidden layers (depth), number of neurons per hidden layer (width), dropout rates (do) [56], and the amount of L_2 regularisation [57].

In order to reduce the dimensions of the architecture space the following choices were made:

- Due to the depth of networks explored, batch normalisation [45] was not considered.
- Having already performed feature selection Sec. 3.1, L_1 regularisation [58] was not considered.
- Rather than adjusting the widths of each layer individually, the widths were allowed to increase or decrease at a constant rate according to the depth of each layer (the *growth rate*), i.e. $w_d = w(1 + dg)$, where w_d is the width of the hidden layer at depth d (zero-ordered), w is the nominal layer width, and g is the growth rate. A growth rate of zero corresponds to constant widths for all layers.
- Dropout layers, when used, were placed after every activation function except the output, and a single rate was used for all dropout layers.

- The same value of L_2 was used for all weight updates.
- Training will use the 1cycle schedule with the same settings used in Sec. 3.8.
- All hidden layers are densely connected as per Sec. 3.9.

Whilst other forms of layer-width growth (quadratic, cubic, *et cetera*) could be considered, we assume that the main issue is to have *some* ability to change the layer widths, rather than the exact parametric form; linear growth offers the simplest form, introducing only one extra hyper-parameter. It should also be mentioned that in initial testing of various architectures, the optimal learning rates were all found to be at about the same point (1×10^{-2}), so the same LR was used for all parameter sampling, in order to reduce the search space by one dimension. The LR can of course be adjusted later for any promising parameter points found.

3.10.2 Parameter scan

While some choices have allowed a reduction of the number of dimensions of the parameter search space, the remaining space still has five dimensions (depth, width, dropout rate, L_2 , and growth rate), meaning a full grid-search of all possible combinations is unfeasible; instead a random search will be used. For each architecture, the following parameter-sampling rules were used:

- Depth sampled from $[2, 9) \in \mathbb{Z}$
- Width sampled from $[33, 101) \in \mathbb{Z}$
- Growth rate sampled from $[-0.2, 1) \in \mathbb{R}$
- L_2 sampled from $\{0, 10^{-2}, 10^{-3}, 10^{-4}, 10^{-5}, 10^{-6}\} \times 10^{-5}$
- Dropout rate sampled from $\{0, 0.05, 0.1, 0.25, 0.5\}$
- The total number of free parameters must be in the range $(5 \times 10^3, 1 \times 10^5)$
- In the case of negative growth rate, the width of the last hidden layer before the output layer must be greater than one.

Just over 350 parameter sets were tested. Each test consisted of training an ensemble of three networks with the specified architecture. The MVAC and MAPA were then calculated and recorded. The testing results were then used to fit Gaussian process models in order to evaluate the partial dependencies of the the metrics on the hyper-parameters. Figure 11 illustrates the distributions of the sampled parameters, and Fig. 12 illustrates the one- and two-dimensional partial dependencies of MVAC and MAPA on the hyper-parameters. Note that the machinery used expects a minimisation problem, hence why the negatives of the metrics are shown.

From the results, the trends in the partial dependencies of both MVAC and MAPA appear to favour minimal explicit regularisation. In terms of depth and width, MVAC shows weak dependence on width and growth rate, and slight dependence on depth, with networks with fewer than four hidden layers performing poorly compared to deeper networks. MAPA again shows weak dependence on width and growth rate, but demonstrates a bounded minima for depth, favouring networks with around five hidden layers.

Figure 13 shows MAPA and MVAC as a function of the total number of free parameters in the networks. From the flat linear-fit, we can see that performance is unrelated to model complexity, and that whilst the data and training methodologies are sufficient for optimising large models, such models are unnecessary to reach better performance.

3.10.3 Further testing

Based on the scan results and partial dependencies, a number of promising parameter sets were further explored with complete trainings, and the LRs set using LR range tests.

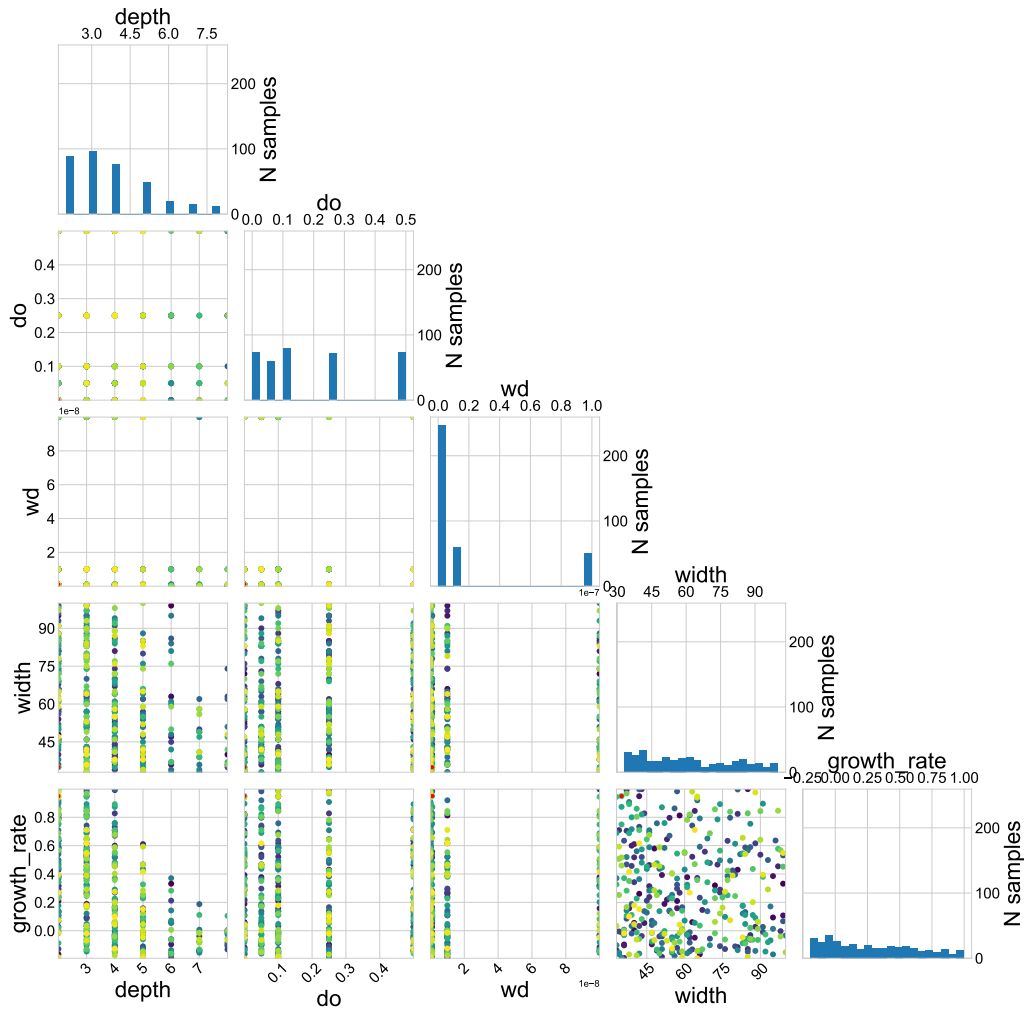


Figure 11: Illustration of the parameter sets sampled during testing.

The performances of these architectures are compared to the current solution (depth 6, width 33, growth rate 0, and no dropout or weight decay) in Tab. 7. As can be seen, none of the new architectures improve on the current architecture in terms of MAPA and although some are able to reach the same level of performance they do not provide significant speed-ups in terms training or inference time.

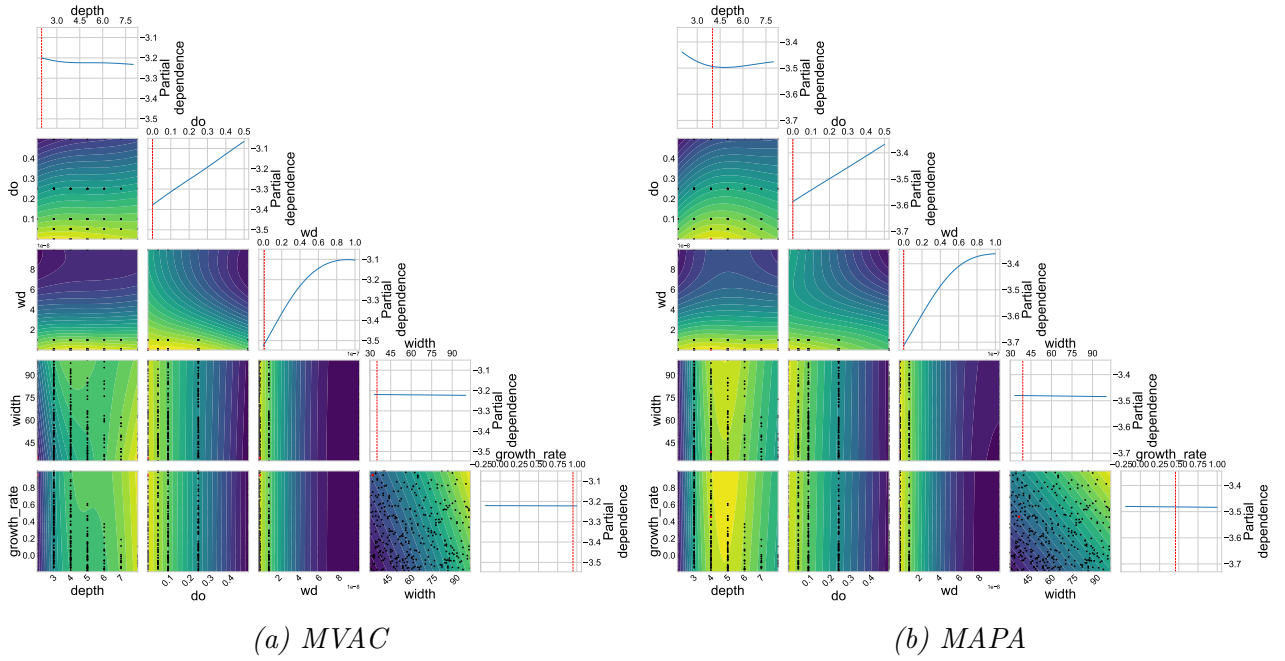


Figure 12: Partial dependencies of negative MVAC and negative MAPA on network hyperparameters. Red indicates the position of the best parameter set found during sampling.

Setup	MMVA	MVAC	MAPA	Fractional time-increase	
				Training	Inference
Current	3.95 ± 0.04	3.89 ± 0.05	3.82 ± 0.02	-	-
4 100 0.1	3.9 ± 0.05	3.83 ± 0.05	3.74 ± 0.01	0.23 ± 0.09	0.6 ± 0.1
4 40 0.45	3.96 ± 0.05	3.90 ± 0.05	3.82 ± 0.01	-0.02 ± 0.05	-0.01 ± 0.03
5 100 -0.1	4.03 ± 0.05	3.91 ± 0.05	3.80 ± 0.02	0.15 ± 0.07	0.6 ± 0.1
5 33 0.9	3.95 ± 0.05	3.89 ± 0.04	3.81 ± 0.02	0.19 ± 0.08	0.6 ± 0.2
8 33 -0.2	3.95 ± 0.06	3.89 ± 0.06	3.82 ± 0.02	0.4 ± 0.1	1.2 ± 0.4

Table 7: Comparison of the various explored architectures. “Current” refers to the solution as of Sec. 3.9. Architectures names are of the form: [depth] [width] [growth rate]. The best values for each metric are shown in bold, and the setup chosen is also indicated in bold.

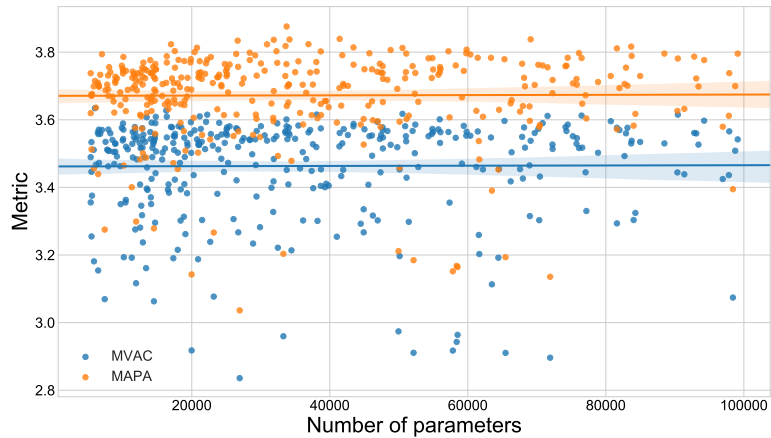


Figure 13: Dependence of the optimisation metrics on the total number of free parameters of the models sampled during testing.

4 Solution evaluation

A comparison between our solution and the existing solutions in terms of performance, timing, and hardware. Our solution is found to match the performance of the winning Kaggle solution whilst being much quicker for train and infer, even on less specialised hardware

4.1 Test results

Having built up a solution using several optimisation metrics and timing changes as guides, we now come to checking the performance of the solution using the remaining metrics: Overall AMS on the public and private portions of the testing data (reminder: MAPA was only an average over subsamples of the public portion of the testing data). In Fig. 14 we show all metrics as a function of solutions developed, averaged over the six trainings that were run per solution. From the results, we can see that whilst MAPA consistently over-estimated actual performance, it's general trend is nonetheless representative of changes in the public and private AMS.

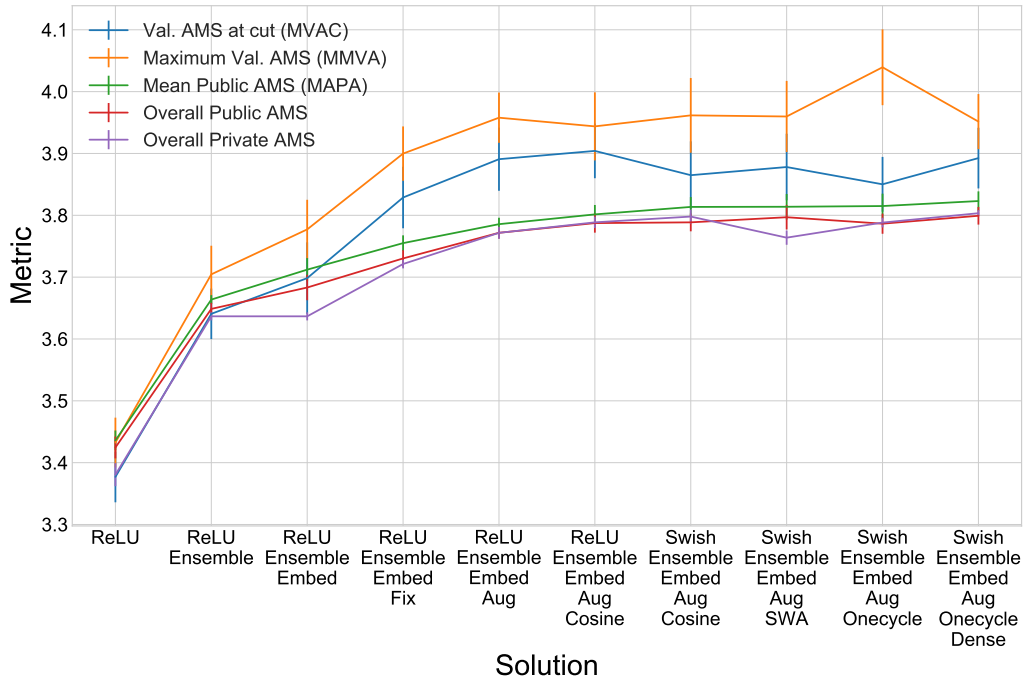


Figure 14: Illustration of the performance metrics for each solution developed.

4.2 Solution timing

Also of interest for real-world application is the time taken by each solution. Plotted in Fig. 15 are the absolute and relative timings for each solution for the variety of hardware tested. Note that one solution was run per hardware configuration, except for the quad-core Xenon setup, which shows the mean of two different machines with the same hardware specification. The numbers in parentheses indicate the number of cores and number of threads per core, respectively, except for the Xenon machines which are cloud-based and are allocated virtual CPUs. From these results, we can see that whilst the GPU is clearly superior, the architectures run sufficiently well on CPU to be viable for use in a particle-physics analysis.

It is also interesting to note the fractional test-time increase for the GPU, which appears to show sub-linear scaling when ensembling, but poor scaling when running inference-time augmentation. This is because LUMIN currently loads each data-fold from the hard-drive into either RAM or VRAM sequentially, and the timing includes this. Once in memory, however, all models in the ensemble are run over the fold. Since the load time for VRAM is non-negligible compared to the prediction time, the fractional increase when evaluating the ten models is much less than nine. Additionally, LUMIN currently applies data-augmentation when loading the data fold, rather than augmenting the data in-place, meaning that the load time is incurred an extra seven times when running TTA, hence the apparent poor scaling when running TTA on a GPU.

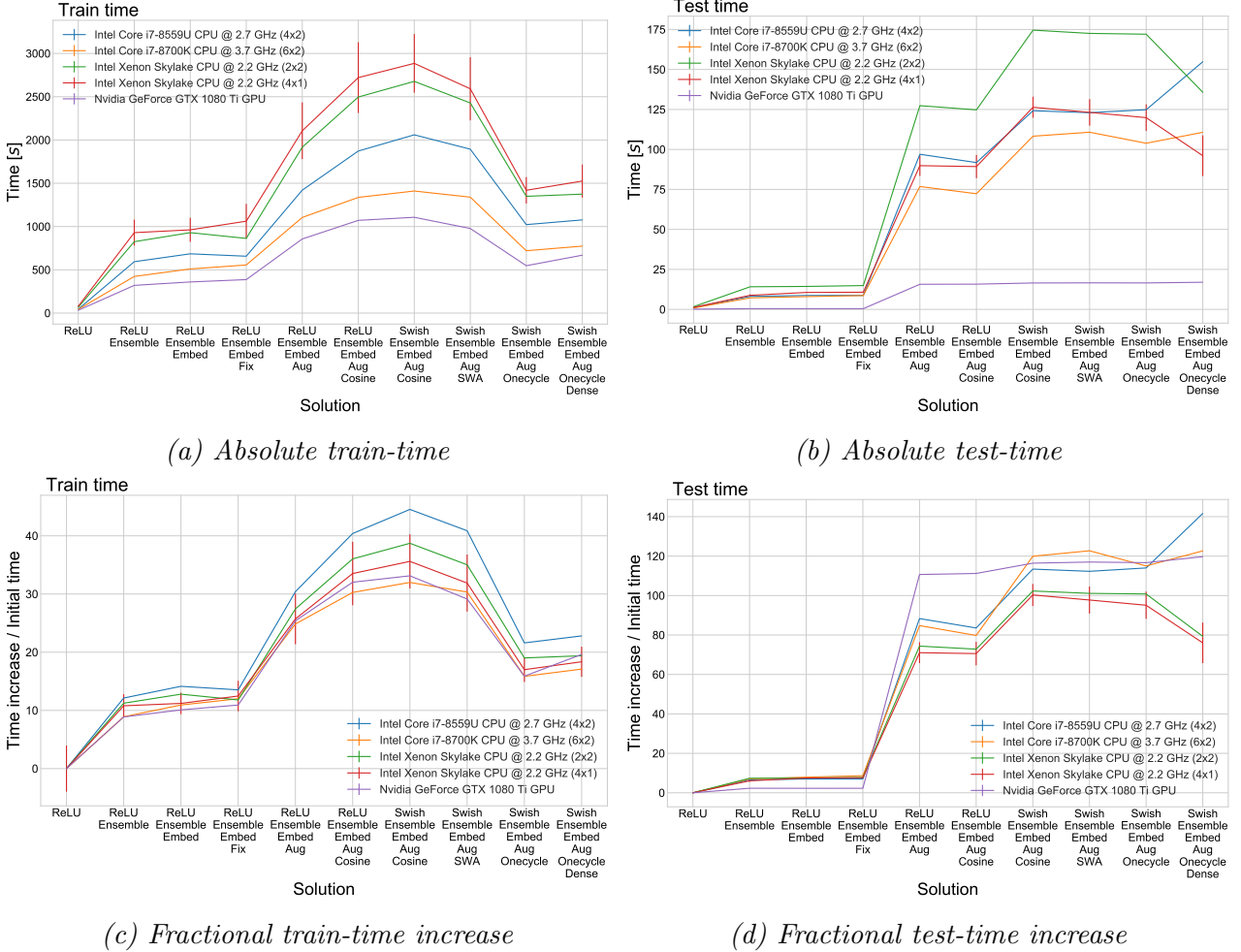


Figure 15: Solution timings for a variety of hardware. Note that the (4x1) Xenon line is an average of two machines, and hence has error bars; only single machines were available for the other hardware configurations and so their associated timing uncertainties cannot be evaluated.

4.3 Discussion

Of the solutions developed, the one from Sec. 3.9 (densely connected network with 1-cycle training scheme) offers the highest values for MAPA, public AMS (3.80 ± 0.01), and private AMS (3.803 ± 0.005), and is also much quicker to train compared to solutions which used constant or cosine-annealed learning-rate schedules.

It was quite surprising that the architecture search performed in Sec. 3.10 was unable to improve on the starting hyper-parameters. The starting architecture (four hidden layers of width 100) was expected to be reasonable based on prior experience with similar

	Our solution	1 st place	2 nd place	3 rd place
Method	10 DNNs	70 DNNs	Many BDTs	108 DNNs
Train-time (GPU)	8 min	12 h	N/A	N/A
Train-time (CPU)	14 min	35 h	48 h	3 h
Test-time (GPU)	15 s	1 h	N/A	N/A
Test-time (CPU)	3 min	???	???	20 min
Score	3.803 ± 0.005	3.80581	3.78913	3.78682

Table 8: Comparison with challenge solutions. ‘N/A’ indicates that the solution was not run on a GPU and so no timing information is available. ‘???’ indicates that the solution was run on CPU but no timing information was reported. Timings for “Our solution” are rounded to the nearest minute, or five seconds. Note that the train times differ to those shown in Fig. 15, which were trained whilst showing a live feedback of the loss to help diagnose any problems, but equated to a constant increase in time per epoch that was independent of the architecture. For the final timings shown here, the live plotting was turned off.

problems and dataset sizes, and the increase to six hidden layers when using densely connected layers was a guess based on factoring in the expected improvement in gradient flow offered by the dense connections and the fact that the layer widths had been reduced by two thirds of the size. It was, however, unlikely to be the most optimal architecture for this specific problem.

As can be seen from the architecture-search results, no explicit regularisation was needed for this problem, and performance was only slightly dependent on the widths of the hidden layers. The rule-of-thumb used to set the initial layer width for the densely connected network (width number = of inputs features (continuous + categorical embeddings)), seems to be appropriate, but further work will be necessary to see how well this rule generalises to other problems and applications.

A comparison to the solutions developed during the running of the challenge is presented in Tab. 8. In terms of hardware, for the solutions developed here, the GPU results are for a Nvidia GeForce GTX 1080 Ti, and the CPU result is for a Intel Core i7-8559U (2018 MacBook Pro). RAM and VRAM usage for each setup was found to be less than 1 GB. Details of the other solutions are as follows:

1. The 1st place solution (available at <https://github.com/melisgl/higgsml>) primarily used a setup with a Nvidia Titan GPU and 24 GB RAM, but Ref. [59] also details timings for an Amazon EC2 m2.4xlarge instance (8-vCPU & 15 GB RAM);
2. The 2nd place solution (<https://github.com/TimSalimans/HiggsML>) was run on an Amazon EC2 m2.4xlarge instance (8-vCPU & 64 GB RAM) and notes the high RAM requirements of the training;
3. And the 3rd place solution used a 2012 quad-core laptop (<https://www.kaggle.com/c/higgs-boson/discussion/10481>).

Even accounting for improvements in hardware and software since 2014, given the uncertainties involved in the metric it would be reasonable to say that the solution developed here achieves comparable performance to winning solutions of the challenge in just a fraction of the time.

5 Conclusion

In this article we have examined several recent advances in deep learning for neural network architectures and training methodologies, and their applicability to a typical prob-

lem in the field of high-energy particle-physics, using data from a popular data-science competition. Whilst the solutions developed were unable to consistently improve on the performance of the winning solutions, they were able to reproduce their performance in a significantly shorter time period using less computational resources.

The solutions were developed in a systematic manner, rather than considering all possible permutations of hyper-parameters, using a variety of metrics (one of which was unavailable during the competition) and considering the time requirements. The improvements to the performance metric are broken down in Fig. 16, where we can see that most of the improvement beyond ensembling (which the winning solutions already used) is coming from domain-specific data augmentation (applied during training and testing). Learning-rate scheduling provides not only a moderate reduction in train time, but also a small improvement in performance. Finally, using densely connected layers offers a further small improvement in performance as well as reducing the dependence of performance on the widths of network layers, potentially making it easier to find optimal architectures for similar applications.

Due to all possible permutations of new methods not being considered, it is plausible that some methods would show a greater or worse relative improvement if testing had been performed in a different order. This could happen for a number of reasons, such as: overlaps in improvements in methods; certain pairs of methods working well together; and the non-linear nature of the scoring metric. Table 9 addresses some these reasons by detailing results from retrainings of solutions in which only one new method was added. Whilst all new methods provide at least minor improvements in isolation, it is interesting to see that data augmentation actually provides a greater improvement than ensembling when applied individually, in comparison to Fig. 16, indicating an overlap in the two methods. Also the use of dense connections on their own provides a smaller benefit than they do in the full solution, implying that they are most useful when applied in conjunction with other methods.

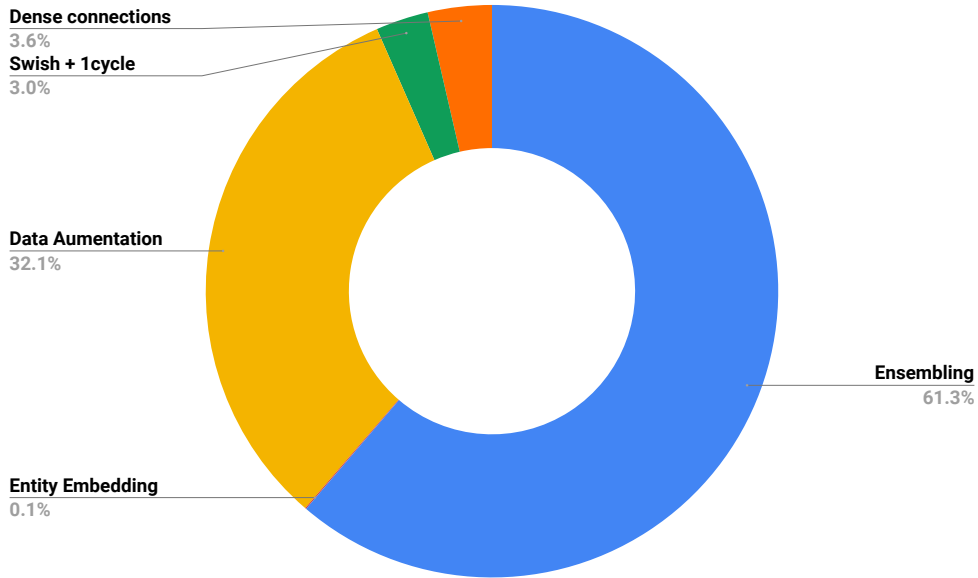


Figure 16: Illustration of the relative contributions of each new method to the overall improvement in mean private AMS over a baseline ReLU model. Note that contributions are calculated sequentially in the order tested, i.e. the entity embedding result includes ensembling, the augmentation result includes embedding and ensembling, et cetera.

Setup	Mean improvement in private AMS
Baseline + Data augmentation	$7.98 \pm 0.05\%$
Baseline + Ensembling	$7.58 \pm 0.05\%$
Baseline + 1cycle	$4.00 \pm 0.03\%$
Baseline + Swish	$2.22 \pm 0.03\%$
Baseline + Embedding	$1.63 \pm 0.03\%$
Baseline + Dense connections	$1.25 \pm 0.03\%$

Table 9: Individual percentage improvements in mean private AMS offered by each new method over a baseline ReLU model. In contrast to Fig. 16 the model setups here do not include other methods, e.g. “Baseline + Embedding” does not also include ensembling.

Acknowledgements

I am very grateful to Michele Gallinaro, Nuno Castro, and João Pedro de Arruda Gonçalves for their valued feedback and comments in reviewing this article, and to the other members of the AMVA4NewPhysics ITN for all the discussions over the years which no doubt helped to contribute to this work. Additional thanks also to the Fast.AI team whose courses introduced me to many of the ideas tested here, as well as inspired me to begin writing my own deep learning framework.

References

- [1] **L3** Collaboration, *Search for the standard model Higgs boson in e^+e^- interactions at $161 \leq s \leq 172 \text{ GeV}$* , Physics Letters B **411** (Oct, 1997)373–386.
[https://doi.org/10.1016/S0370-2693\(97\)01033-2](https://doi.org/10.1016/S0370-2693(97)01033-2).
- [2] **DØ** Collaboration, *Search for single top quark production at $D\bar{\nu}$ using neural networks*, Physics Letters B **517** no. 3, (2001)282 – 294.
<http://www.sciencedirect.com/science/article/pii/S0370269301010097>.
- [3] **CMS** Collaboration, *A search using multivariate techniques for a standard model Higgs boson decaying into two photons*, Tech. Rep. CMS-PAS-HIG-12-001, CERN, Geneva, 2012. <https://cds.cern.ch/record/1429931>.
- [4] **ATLAS** Collaboration, *Observation of a new particle in the search for the Standard Model Higgs boson with the ATLAS detector at the LHC*, Physics Letters B **716** no. 1, (Sep, 2012) 1–29. <http://dx.doi.org/10.1016/j.physletb.2012.08.020>.
- [5] **CMS** Collaboration, *Observation of a new boson at a mass of 125 GeV with the CMS experiment at the LHC*, Physics Letters B **716** no. 1, (Sep, 2012) 30–61.
<http://dx.doi.org/10.1016/j.physletb.2012.08.021>.
- [6] A. Graves and J. Schmidhuber, *Offline Handwriting Recognition with Multidimensional Recurrent Neural Networks*, Advances in Neural Information Processing Systems **22** (2009)545–552.
<http://people.idsia.ch/~juergen/nips2009.pdf>.
- [7] G. E. Dahl, D. Yu, L. Deng, and A. Acero, *Large vocabulary continuous speech recognition with context-dependent DBN-HMMS*, 2011 IEEE International Conference on Acoustics, Speech and Signal Processing (ICASSP) (2011)4688–4691.
- [8] K. Albertsson *et al.*, *Machine Learning in High Energy Physics Community White Paper*, 2018.
- [9] M. Andrews, M. Paulini, S. Gleyzer, and B. Poczós, *End-to-End Physics Event Classification with the CMS Open Data: Applying Image-based Deep Learning on Detector Data to Directly Classify Collision Events at the LHC*, [arXiv:1807.11916](https://arxiv.org/abs/1807.11916) [hep-ex].
- [10] M. Paganini, L. de Oliveira, and B. Nachman, *CaloGAN : Simulating 3D high energy particle showers in multilayer electromagnetic calorimeters with generative adversarial networks*, Phys. Rev. **D97** no. 1, (2018) 014021, [arXiv:1712.10321](https://arxiv.org/abs/1712.10321) [hep-ex].
- [11] **CMS** Collaboration, *Heavy flavor identification at CMS with deep neural networks*, CMS-DP-2017-005 (Mar, 2017). <https://cds.cern.ch/record/2255736>.
- [12] J. Deng *et al.*, *ImageNet: A Large-Scale Hierarchical Image Database*, in *CVPR09*. 2009.
- [13] **ATLAS** Collaboration, *Dataset from the ATLAS Higgs Boson Challenge 2014*, CERN Open Data Portal (2014).
- [14] C. Adam-Bourdarios *et al.*, *The Higgs boson machine learning challenge*, JMLR: Workshop and Conference Proceedings **42** (2015).
- [15] L. Evans and P. Bryant, *LHC Machine*, JINST **3** (2008) S08001.
- [16] A. L. Read, *Presentation of search results: the CLs technique*, Journal of Physics G: Nuclear and Particle Physics **28** no. 10, (sep, 2002)2693–2704.
<https://doi.org/10.1088/0954-3899/28/10/313>.
- [17] A. Buckley *et al.*, *General-purpose event generators for LHC physics*, Phys. Rept. **504** (2011)145–233, [arXiv:1101.2599](https://arxiv.org/abs/1101.2599) [hep-ph].

- [18] T. Chen and C. Guestrin, *XGBoost: A Scalable Tree Boosting System*, CoRR **abs/1603.02754** (2016). <http://arxiv.org/abs/1603.02754>.
- [19] J. Allison *et al.*, *Geant4 developments and applications*, IEEE Transactions on Nuclear Science **53** no. 1, (Feb, 2006)270–278.
- [20] S. Agostinelli *et al.*, *Geant4—a simulation toolkit*, Nucl. Instr.Meth. A **506** no. 3, (2003)250 – 303.
<http://www.sciencedirect.com/science/article/pii/S0168900203013688>.
- [21] **ATLAS** Collaboration, *The ATLAS Experiment at the CERN Large Hadron Collider*, J. Instrum. **3** (2008) S08003. 437. Also published by CERN Geneva in 2010.
- [22] R. Johnson and T. Zhang, *Learning Nonlinear Functions Using Regularized Greedy Forest*, ArXiv e-prints (Sept., 2011), [arXiv:1109.0887](https://arxiv.org/abs/1109.0887) [stat.ML].
- [23] G. Cowan, *Two developments in tests for discovery: use of weighted Monte Carlo events and an improved measure*, Progress on Statistical Issues in Searches, SLAC (2012).
- [24] B. Sun *et al.*, *SuperTML: Two-Dimensional Word Embedding and Transfer Learning Using ImageNet Pretrained CNN Models for the Classifications on Tabular Data*, CoRR **abs/1903.06246** (2019), [arXiv:1903.06246](https://arxiv.org/abs/1903.06246).
<http://arxiv.org/abs/1903.06246>.
- [25] **ATLAS** Collaboration, *Dataset from the ATLAS Higgs Boson Machine Learning Challenge 2014*, CERN Open Data Portal (2014).
- [26] **AMVA4NewPhysics** Collaboration, *Classification and Regression Tools in Higgs Measurements*, tech. rep., Oct, 2018.
<https://docs.infn.it/share/s/c9veKvvtT3-WmoC6TW66jQ>.
- [27] L. Breiman, *Random Forests*, Mach. Learn. **45** no. 1, (Oct., 2001)5–32.
<https://doi.org/10.1023/A:1010933404324>.
- [28] *Spearman Rank Correlation Coefficient*, pp. 502–505. Springer New York, New York, NY, 2008. https://doi.org/10.1007/978-0-387-32833-1_379.
- [29] G. C. Strong, *LUMIN*, Mar., 2019. <https://doi.org/10.5281/zenodo.2601857>. Please check <https://github.com/GilesStrong/lumin/graphs/contributors> for the full list of contributors.
- [30] K. He, X. Zhang, S. Ren, and J. Sun, *Delving Deep into Rectifiers: Surpassing Human-Level Performance on ImageNet Classification*, CoRR **abs/1502.01852** (2015). <http://arxiv.org/abs/1502.01852>.
- [31] R. Arora, A. Basu, P. Mianjy, and A. Mukherjee, *Understanding Deep Neural Networks with Rectified Linear Units*, CoRR **abs/1611.01491** (2016).
<http://arxiv.org/abs/1611.01491>.
- [32] X. Glorot and Y. Bengio, *Understanding the difficulty of training deep feedforward neural networks*, JMLR Workshop and Conference Proceedings **9** (2010).
<http://jmlr.org/proceedings/papers/v9/glorot10a/glorot10a.pdf>.
- [33] D. E. Rumelhart, G. E. Hinton, and R. J. Williams, *Learning representations by back-propagating errors*, Nature **323** (Oct., 1986)533–536.
- [34] D. P. Kingma and J. Ba, *Adam: A Method for Stochastic Optimization*, CoRR **abs/1412.6980** (2014), [arXiv:1412.6980](https://arxiv.org/abs/1412.6980). <http://arxiv.org/abs/1412.6980>.
- [35] L. N. Smith, *No More Pesky Learning Rate Guessing Games*, CoRR **abs/1506.01186** (2015), [arXiv:1506.01186](https://arxiv.org/abs/1506.01186).
- [36] C. Guo and F. Berkhahn, *Entity Embeddings of Categorical Variables*, CoRR **abs/1604.06737** (2016), [arXiv:1604.06737](https://arxiv.org/abs/1604.06737).
<http://arxiv.org/abs/1604.06737>.

- [37] fast.ai, *Practical Deep Learning For Coders, Part 1 Lesson 4*, 2018. course18.fast.ai/lessons/lesson4.html. Accessed 2019/05/06.
- [38] CMS Collaboration, *The CMS Experiment at the CERN LHC*, JINST **3** (2008) S08004.
- [39] A. Krizhevsky, I. Sutskever, and G. E. Hinton, *ImageNet Classification with Deep Convolutional Neural Networks*, in *Advances in Neural Information Processing Systems 25: 26th Annual Conference on Neural Information Processing Systems 2012. Proceedings of a meeting held December 3-6, 2012, Lake Tahoe, Nevada, United States.*, pp. 1106–1114. 2012. <http://papers.nips.cc/paper/4824-imagenet-classification-with-deep-convolutional-neural-networks>.
- [40] Y. Bengio, *Practical recommendations for gradient-based training of deep architectures*, CoRR **abs/1206.5533** (2012), arXiv:1206.5533. <http://arxiv.org/abs/1206.5533>.
- [41] K. He, X. Zhang, S. Ren, and J. Sun, *Deep Residual Learning for Image Recognition*, CoRR **abs/1512.03385** (2015), arXiv:1512.03385. <http://arxiv.org/abs/1512.03385>.
- [42] I. Loshchilov and F. Hutter, *SGDR: Stochastic Gradient Descent with Restarts*, CoRR **abs/1608.03983** (2016), arXiv:1608.03983. <http://arxiv.org/abs/1608.03983>.
- [43] G. Huang *et al.*, *Snapshot Ensembles: Train 1, get M for free*, CoRR **abs/1704.00109** (2017), arXiv:1704.00109. <http://arxiv.org/abs/1704.00109>.
- [44] G. Klambauer, T. Unterthiner, A. Mayr, and S. Hochreiter, *Self-Normalizing Neural Networks*, CoRR **abs/1706.02515** (2017). <http://arxiv.org/abs/1706.02515>.
- [45] S. Ioffe and C. Szegedy, *Batch Normalization: Accelerating Deep Network Training by Reducing Internal Covariate Shift*, Stanford University, Tech. Rep. (2015). <http://jmlr.org/proceedings/papers/v37/ioffe15.pdf>.
- [46] Y. LeCun, L. Bottou, G. Orr, and K.-R. Müller, *Efficient Backprop.*, <http://yann.lecun.com/exdb/publis/pdf/lecun-98b.pdf>.
- [47] P. Ramachandran, B. Zoph, and Q. V. Le, *Searching for Activation Functions*, CoRR **abs/1710.05941** (2017), arXiv:1710.05941. <http://arxiv.org/abs/1710.05941>.
- [48] T. Garipov, P. Izmailov, D. Podoprikin, D. Vetrov, and A. G. Wilson, *Loss Surfaces, Mode Connectivity, and Fast Ensembling of DNNs*, ArXiv e-prints (Feb., 2018), arXiv:1802.10026 [stat.ML].
- [49] F. Draxler, K. Veschgini, M. Salmhofer, and F. A. Hamprecht, *Essentially No Barriers in Neural Network Energy Landscape*, ArXiv e-prints (Mar., 2018), arXiv:1803.00885 [stat.ML].
- [50] P. Izmailov, D. Podoprikin, T. Garipov, D. P. Vetrov, and A. G. Wilson, *Averaging Weights Leads to Wider Optima and Better Generalization*, CoRR **abs/1803.05407** (2018), arXiv:1803.05407. <http://arxiv.org/abs/1803.05407>.
- [51] L. N. Smith and N. Topin, *Super-Convergence: Very Fast Training of Residual Networks Using Large Learning Rates*, CoRR **abs/1708.07120** (2017), arXiv:1708.07120. <http://arxiv.org/abs/1708.07120>.
- [52] L. N. Smith, *A disciplined approach to neural network hyper-parameters: Part 1 - learning rate, batch size, momentum, and weight decay*, CoRR **abs/1803.09820** (2018), arXiv:1803.09820. <http://arxiv.org/abs/1803.09820>.

- [53] fast.ai, *fastai library documentation*, 2019. docs.fast.ai/. Accessed 2019/05/13.
- [54] G. Huang, Z. Liu, and K. Q. Weinberger, *Densely Connected Convolutional Networks*, CoRR [abs/1608.06993](https://arxiv.org/abs/1608.06993) (2016), [arXiv:1608.06993](https://arxiv.org/abs/1608.06993).
<http://arxiv.org/abs/1608.06993>.
- [55] C.-Y. Lee, S. Xie, P. Gallagher, Z. Zhang, and Z. Tu, *Deeply-Supervised Nets*, arXiv e-prints (Sep, 2014) [arXiv:1409.5185](https://arxiv.org/abs/1409.5185), [arXiv:1409.5185](https://arxiv.org/abs/1409.5185) [stat.ML].
- [56] N. Srivastava, G. Hinton, A. Krizhevsky, I. Sutskever, and R. Salakhutdinov, *Dropout: A Simple Way to Prevent Neural Networks from Overfitting*, Journal of Machine Learning Research **15** (2014)1929–1958.
<http://jmlr.org/papers/v15/srivastava14a.html>.
- [57] A. Y. Ng, *Feature selection, L1 vs. L2 regularization, and rotational invariance*, ICML (2004).
<https://icml.cc/Conferences/2004/proceedings/papers/354.pdf>.
- [58] R. Tibshirani, *Regression Shrinkage and Selection via the Lasso*, Journal of the Royal Statistical Society. Series B (Methodological) **58** no. 1, (1996)267–288.
<http://www.jstor.org/stable/2346178>.
- [59] G. Melis, *Dissecting the winning solution of the higgsml challenge*, JMLR: Workshop and Conference Proceedings **42** (2015).
- [60] H. Cheng *et al.*, *Wide & Deep Learning for Recommender Systems*, CoRR [abs/1606.07792](https://arxiv.org/abs/1606.07792) (2016), [arXiv:1606.07792](https://arxiv.org/abs/1606.07792).
<http://arxiv.org/abs/1606.07792>.
- [61] A. Paszke *et al.*, *Automatic Differentiation in PyTorch*, in *NIPS Autodiff Workshop*. 2017.
- [62] T. Augspurger *et al.*, *seaborn: v0.7.1 (June 2016)*, June, 2016.
<https://doi.org/10.5281/zenodo.54844>.
- [63] J. D. Hunter, *Matplotlib: A 2D graphics environment*, Computing In Science & Engineering **9** no. 3, (2007)90–95.
- [64] W. McKinney, *Data Structures for Statistical Computing in Python*, in *Proceedings of the 9th Python in Science Conference*, S. van der Walt and J. Millman, eds., pp. 51 – 56. 2010.
- [65] S. van der Walt, S. C. Colbert, and G. Varoquaux, *The NumPy Array: A Structure for Efficient Numerical Computation*, Computing in Science Engineering **13** no. 2, (March, 2011)22–30.
- [66] M. Brucher *et al.*, *Scikit-learn: Machine Learning in Python*, Journal of Machine Learning Research **12** (2011)2825–2830.
- [67] T. Parr and K. Turgutlu, *Feature importances for scikit random forests.*
<https://github.com/parrt/random-forest-importances>. See also
<https://explained.ai/rf-importance/index.html>.
- [68] T. Head *et al.*, *scikit-optimize/scikit-optimize: v0.5.2*, Mar., 2018.
<https://doi.org/10.5281/zenodo.1207017>.

Appendices

A Parallel networks and feature splitting

An investigation into more complex architectures which split the input features along separate processing paths. Whilst this section does not result in an improvement, it does illustrate how these architectures can be used to further interpret the data and so has been included as an appendix to the main report. In the course of solution development, this investigation took place just prior to the architecture search detailed in Sec. 3.10.

So far we have treated all the input features in the same manner (aside from embedding the jet multiplicity) and passed them all through the networks together. However, in particle physics we have lower-level features, such as final-state 4-momenta, but we often compute several high-level features, which are theory inspired non-linear combinations of low-level features, such as the Higgs mass. Indeed, the Higgs ML dataset contains both high (DER) and low (PRI) features.

As was shown in Fig. 1, the high-level features in the data already demonstrate a good degree of class separation compared to the low-level features. Because of this, it is possible that we could reduce the number of free parameters of the model; although the low-level features might require a deeper network to learn a useful representation for them, perhaps the high-level features might simply require a single layer to encode them. Such architectures have been referred to in literature as *Wide & Deep learning*, e.g. Ref. [60].

It is likely, however that the optimal model will require some interactions between the high- and low-level features. We can consider two extra architectures in addition to completely splitting the features: In the first architecture, all of the input features are passed through the deep network as normal, but additionally the high-level features are passed through a single layer which is then concatenated with the output of the deep block. In this case the single layer can encode easily the high-level information, allowing the deep block to learn to represent better the low-level information and to capture the interactions between the low- and high-level features.

In the second architecture, the low- and high-level features are split, but two *bottleneck* layers are used to encode a low-dimensional representation of the sets of features. The outputs of the bottleneck layers are then concatenated with their opposite set of features to provide inputs to each block: i.e. the compressed representation of the high-level features is concatenated with the low-level features and passed to the deep block, and vice versa. In this case, the bottleneck layers should learn the most useful representation of the information which each network block would otherwise not have available, whilst still allowing the number of free parameters in the model to be comparatively small.

A.0.1 Testing

Three architectures were tested:

1. Full-split: The low-level features were passed through a six-layer-deep, 20 neuron-wide, densely connected set of hidden layers, and the high-level features were passed through a single 50-neuron-wide layer. 9303 free parameters.
2. Full-split+bottlenecks: Each set of low- and -high level features are passed through single neuron bottleneck layers. The low-level features, concatenated with the high-level-bottleneck output, were passed through a six-layer-deep, 21 neuron-wide, densely connected set of hidden layers, and the high-level features were concatenated with the low-level-bottleneck output and passed through a single 51-neuron-wide layer. 10 272 free parameters.

3. Semi-split: Both the low and high level features are passed through a six-layer-deep, 33 neuron-wide, densely connected set of hidden layers, and additionally the high-level features were passed through a single 50-neuron-wide layer. 23 863 free parameters.

In all cases, Swish activation functions were placed after every linear layer, and the outputs of the wide and deep blocks were then concatenated and passed through the output neuron. Figure 17 illustrates the three network architectures. For reference the current solution as of Sec. 3.9 uses 23 113 free parameters.

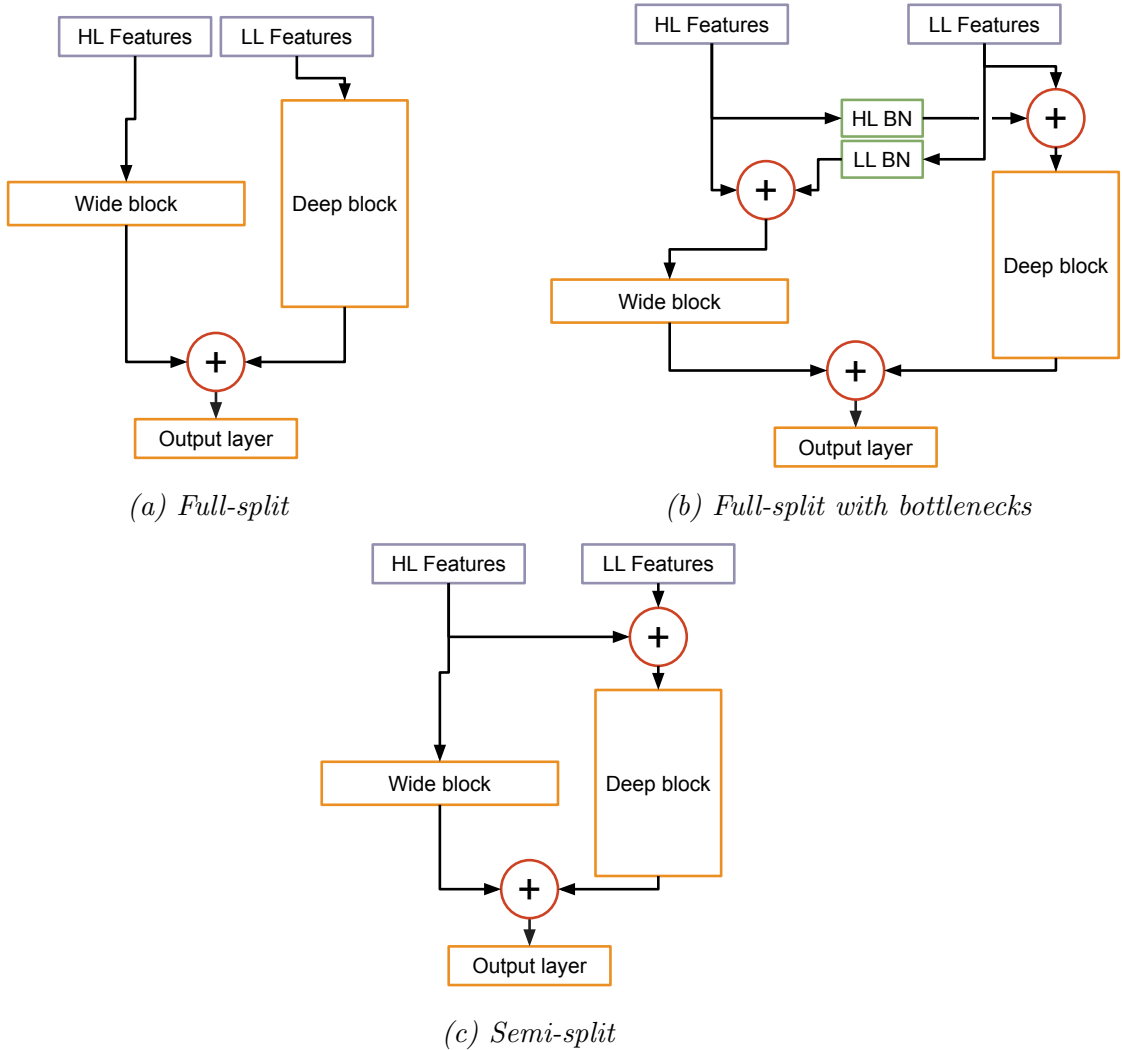


Figure 17: Architecture diagrams for the parallel networks considered. \oplus indicates concatenations of hidden states, BN stands for “bottleneck”, and HL and LL stand for “high-level” and “low-level”, respectively.

From Tab. 10, we can see that completely splitting the features severely reduces model performance, but that allowing the network to learn compressed representations of the features goes some way to recover performance. We can also see that the addition of the linear embedding for high-level features, offered by the semi-split architecture does not provide any improvement over the current solution, and only serves to increase the model size and timings.

Setup	MMVA	MVAC	MAPA	Fractional time-increase	
				Training	Inference
Current	3.95 ± 0.04	3.89 ± 0.05	3.82 ± 0.02	-	-
Full-split	3.69 ± 0.06	3.64 ± 0.06	3.596 ± 0.006	0.02 ± 0.03	-0.10 ± 0.04
Full-split+BN	3.80 ± 0.05	3.72 ± 0.05	3.647 ± 0.006	0.14 ± 0.05	0.00 ± 0.05
Semi-split	3.93 ± 0.05	3.86 ± 0.05	3.82 ± 0.02	0.12 ± 0.02	0.1 ± 0.1

Table 10: Comparison of the various parallel network architectures. “Current” refers to the solution as of Sec. 3.9. ‘BN’ in this case stands for BottleNeck. The best values for each metric are shown in bold, and the setup chosen is also indicated in bold.

A.0.2 Interpretation

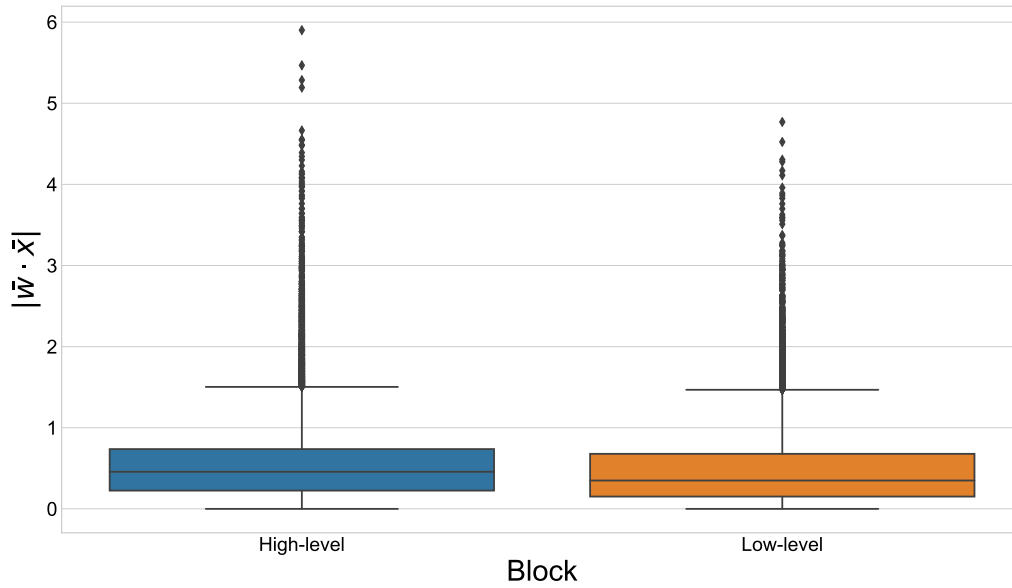
Whilst it was found that none of the parallel architectures provided improvements over the current solution, they do allow for several informative interpretation methods due to the fact that the features are being split into subgroups.

Since the output layer in each model consists of a single neuron which directly takes its inputs from the wide and deep block outputs, we can compute the absolute values of the dot products of slices of the output neuron’s weights with the corresponding inputs from each of the wide and deep blocks for a range of data points. This then gives an idea of the reliance of the model’s prediction on particular subsets of inputs.

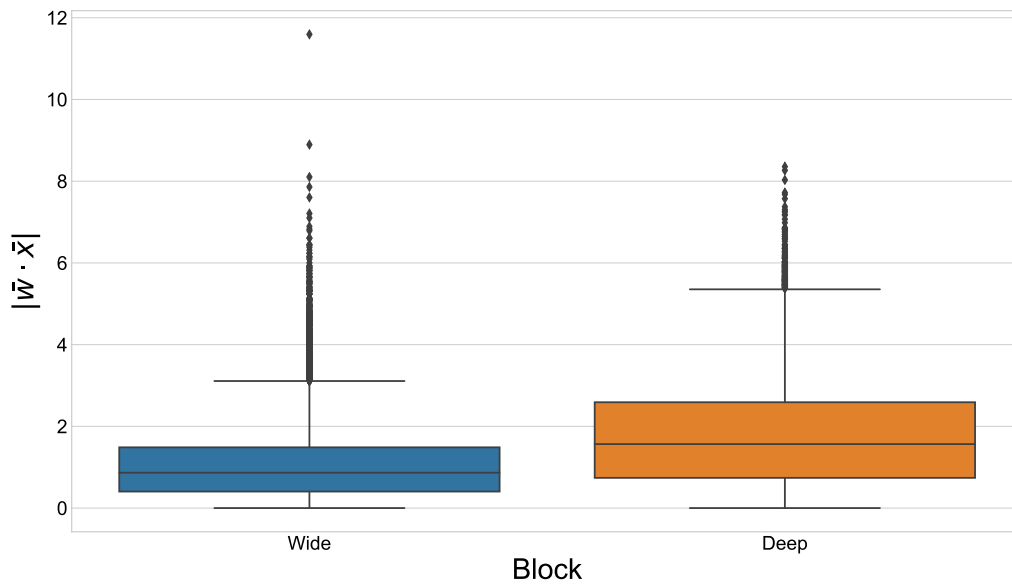
From Fig. 18 we can see that the “Full-split” architecture shows a slightly higher dependence on the single layer fed with the high-level features, but the fact that this difference in dependence is only minor suggests that the deep block is learning a powerful representation of the low-level features. The “Semi-split” model, on the other hand, shows a strong reliance on the deep block (which contains both high and low features), confirming the result that the single-layer embedding of the high-level features does not add much to the model performance.

In a similar fashion, the bottleneck layers of the “Full-split+bottlenecks” architecture can be interpreted by computing the absolute values of the weights times the feature values for a range of data points. Comparing Fig. 19b to Fig. 2, we can see that the high-level bottleneck representation does not rely mostly on the two most important features (the MMC mass and the transverse mass), but instead focusses on some weaker features, such as $p_{t,h}$ and $\sum p_t$. This is perhaps an indication that the the MMC mass and the transverse mass are already strong enough features, and instead the deep block is being used to refine some of the weaker high-level features by combining them with low-level information. It is also interesting to note in Fig. 19a that the low-level bottleneck appears to be used for passing information about jet multiplicity and missing transverse energy; features which could potentially be used to parametrise the response of the wide layer to the jet-related features.

As a final stage of interpretation of the bottleneck layers, we can plot the distributions of the their outputs for a range of data points (Fig. 20). We can see that both bottlenecks learn features which display decent separation between the data classes.

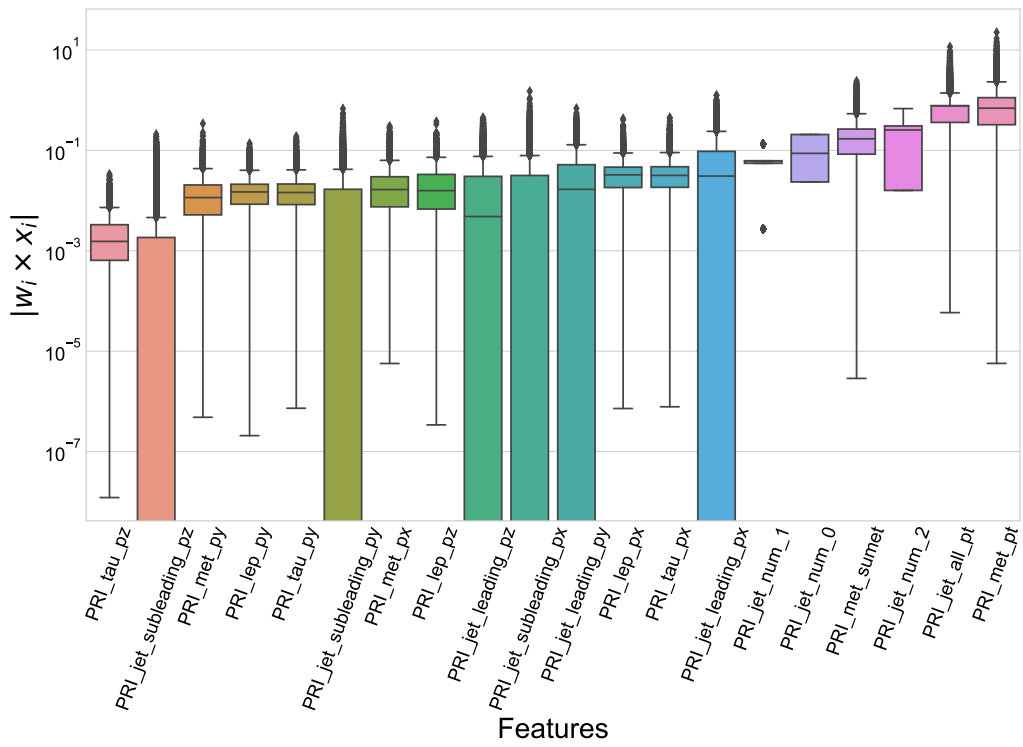


(a) Model reliance on high-level and low-level features as processed by the “Full-split” architecture.

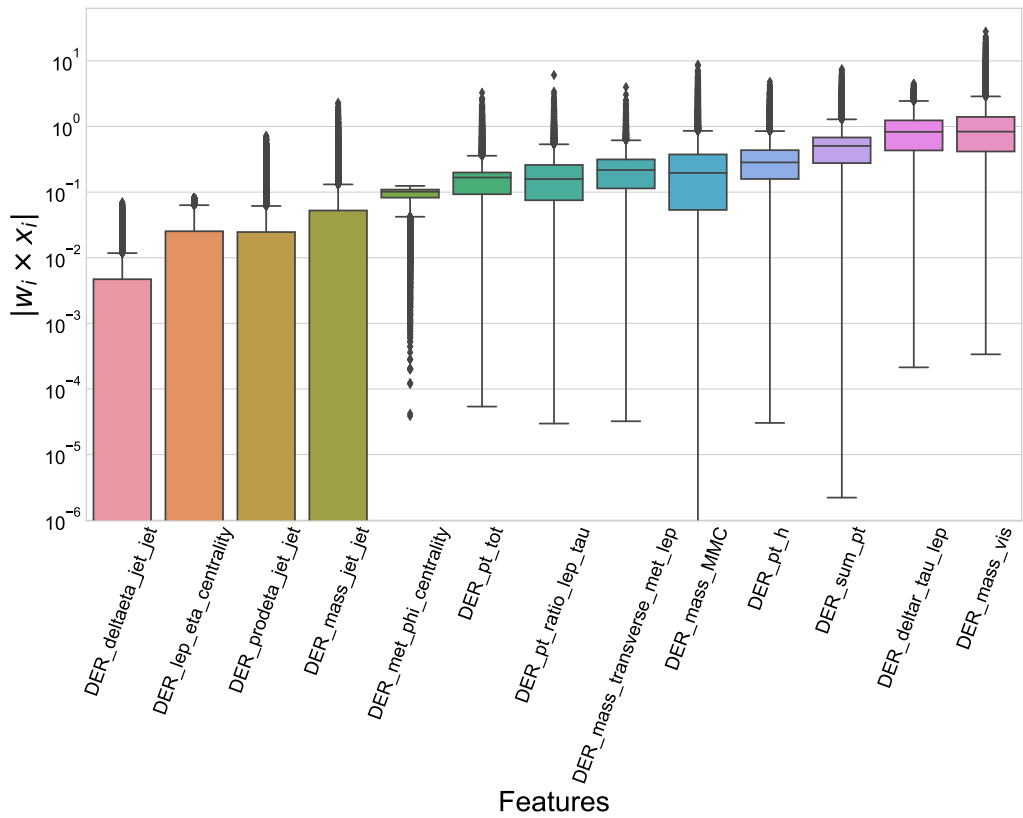


(b) Model reliance on high-level and high+low-level features as processed by the “Semi-split” architecture.

Figure 18: Model reliance on subsets of features

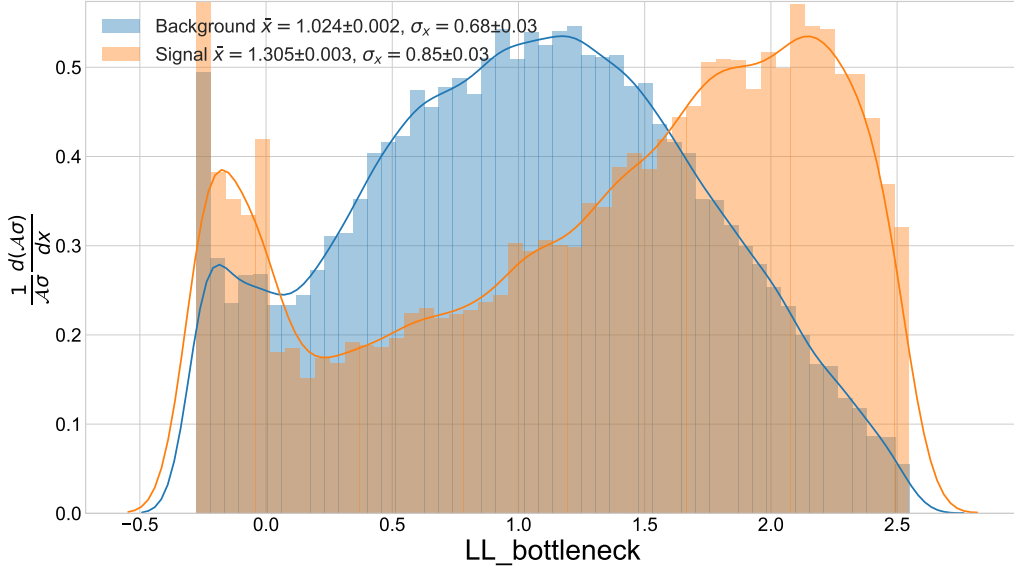


(a) Low level

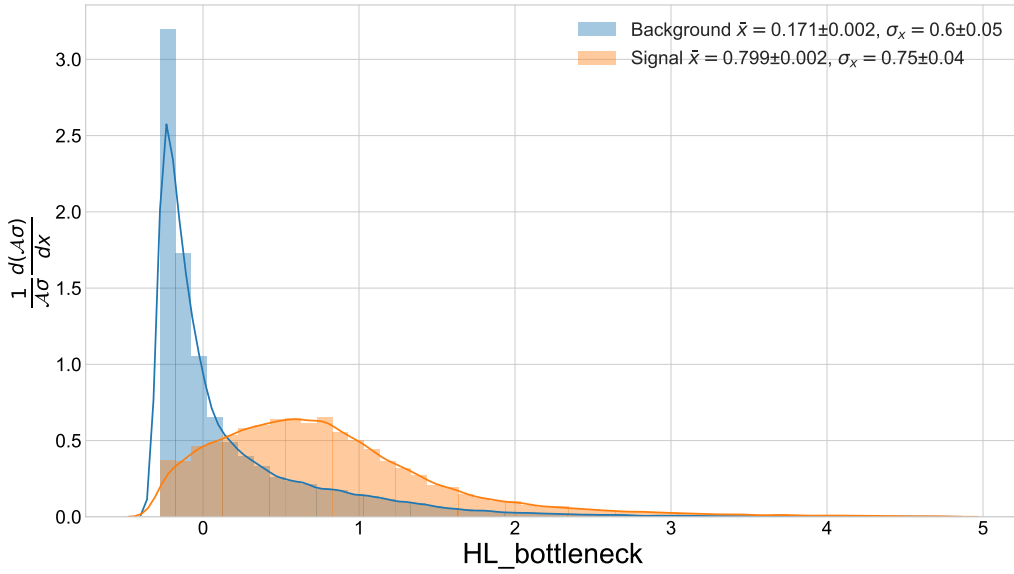


(b) High level

Figure 19: Bottleneck reliance on individual features.



(a) Low level



(b) High level

Figure 20: Output distribution of the bottleneck layers separated by event class. *N.B.* These are the outputs after the activation layers of the bottlenecks. It is interesting to note the “double-peak” distribution of the low-level bottleneck output; further inspection revealed that the peak close to zero was only present in events containing at least one jet, further supporting the hypothesis that the low-level bottleneck learns to pass jet-multiplicity information to the wide-block.

B Software details

The investigation performed in this article made use of several packages, which are detailed in Tab. 11. The framework and notebook experiments are made available at https://github.com/GilesStrong/HiggsML_Lumin.

Software	Version	References	Use/Notes
LUMIN	0.0.0-0.3.1	[29]	Wrapping PYTORCH to implement new methods presented
PYTORCH	1.0.0	[61]	Implementing neural networks
SEABORN	0.8.1	[62]	Plot production
MATPLOTLIB	3.0.2	[63]	Plot production
PANDAS	0.23.4	[64]	Data analysis and computation
NUMPY	1.15.2	[65]	Data analysis and computation
SCIKIT-LEARN	0.20.0	[66]	Cross-validation and pre-processing
RFIMP	1.3.4	[67]	Random Forest Permutation Importance and mutual dependency calculations
SCIKIT-OPTIMIZE	0.5.2	[68]	GP fitting and hyper-parameter partial-dependence calculations

Table 11: Software used for the investigation